# Downward opposed flame spread response to non-steady airflow.

By Alana C. Miska

A Master's Thesis

Submitted to the Faculty of

WORCESTER POLYTECHNIC INSTITUTE

In partial fulfillment of the requirements for the

Degree of Master of Science in Fire Protection Engineering

Report Submitted to: Professor James Urban

Worcester Polytechnic Institute (WPI)

7/30/2024

Approved:

________________________________

Professor James Urban, Advisor

________________________________

Professor Ali Rangwala

________________________________

Dr. Maria Thomsen

# Acknowledgements

I would first like to express my gratitude to my thesis advisor, Dr. James Urban, for his guidance and support throughout the project. His expertise and mentorship have been crucial in shaping the direction of this work and allowing me to grow in my academic and professional life.

Special thanks to my fellow researchers in WPI's Fire Protection Engineering Department who helped me along the way, particularly Pablo Pinto, Xiuqi Xi and the entirety of the Urban Research Group. Our collaborations and insightful discussions have been incredibly valuable to my academics and research and are greatly appreciated.

I would also like to thank Frederick Brokaw for his technical support in the FPE Lab. His guidance and training to safely and successfully construct the wind tunnel was instrumental in performing quality experiments.

In addition, I would like to thank Diane Poirier, Administrative Assistant at WPI, for her immense support of all FPE students. Her encouragement and support have made a significant impact on my time as a graduate student at WPI.

I would also like to thank the National Science Foundation (NSF) for their generous funding of this project through award #2126467.

Lastly, I would like to express my immense gratitude to my family and friends for always providing me with encouragement and support. They have been a constant source of strength and motivation throughout my academic journey at WPI.

# Abstract

PMMA is burned in a bench scale wind tunnel under steady and oscillating airflows to characterize the downward flame spread response to non-steady airflow conditions. An opposed forced flow configuration is used with 0.5 and 1 mm thick black cast PMMA. The non-steady airflow oscillations for both PMMA thicknesses take the form of a transient sinusoidal profile with three amplitudes (0.1, 0.15 and 0.2 m/s), three frequencies (1/8, 1/16 and 1/32 Hz) and one baseline airflow (0.45 m/s). The time averaged and transient flame spread rate are measured using the change in pyrolysis front over time. The frequency response of the flame behavior, flame length and flame spread rate due to the impact of the non-steady airflow are investigated. A transient gas phase response is seen in all forced flow conditions. The smaller sample thickness displayed a clearer response in the transient flame spread to the non-steady airflow. This behavior is analyzed using physical timescales for solid phase heating.

# Table of Contents

# List of Figures

## List of Tables

# 1. Introduction

Flame spread is a critical characteristic in the growth of a fire in both urban and wildland settings. Many efforts have been made to understand the key variables that impact flame spread, such as fuel compositions and configurations, wind interaction and ambient conditions [1], [2], [3], [4], [5]. However, most of these efforts consider steady conditions, such as a steady (or time-averaged) wind/airflow and a steady (or time-averaged) rate of spread. This is not fully representative of the transient and dynamic flame behaviors seen in real fires and few studies to date have characterized this non-steady action.

An example of non-steady behavior in the urban setting was seen in the Londen Grenfell Tower Fire in 2017. This tragic event resulted in 72 fatalities, largely in part to rapid spread over the building façade. Using a wide selection of verified video and photographic data from the fire, Guillaume et.al. tracked the vertical spread of the fire over time [6], as shown in Figure 1 below. The results of this study show that the spread was not steady. Instead, it was separated into three individual trends. The initial rate of growth is relatively linear, then there is a deceleration in spread rate, and finally the flame accelerates exponentially until it reaches the top of the building.

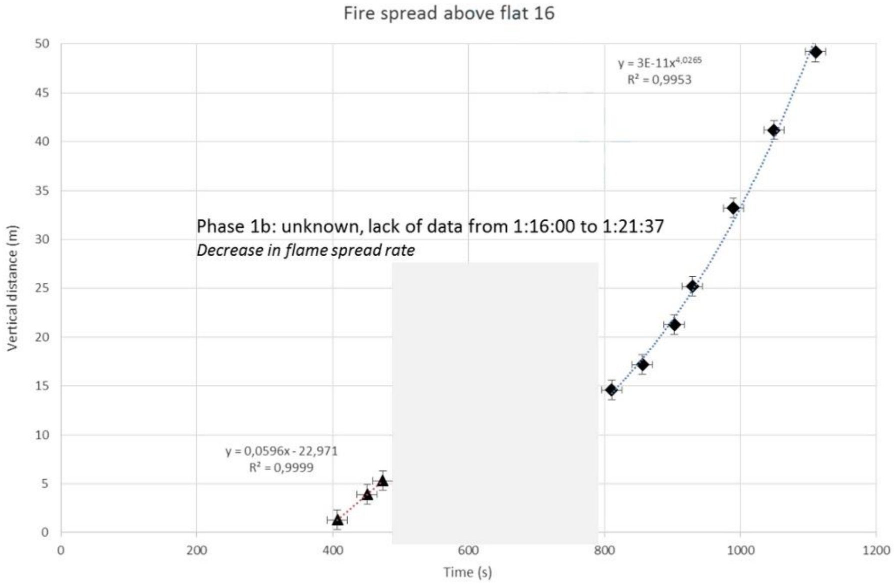

*Figure 1.* Vertical flame spread over time of the Grenfell Tower Fire, reported by Guillaume et.al. [6].

Another place flame instabilities are found in urban settings is in flashover of a compartment fire. One mechanism causing flashover is the rapid acceleration of flame spread just before the fire is fully developed [7][8]. These are all examples of flame spread characteristics that are transient in nature but are often described in a "quasi-steady" method.

Another important and crucial motivator for better understanding fire spread mechanisms is wildfire prevention and management strategies. Wildfires are complex and dynamic flames that are influenced by many factors, such as weather, topography, and intricate fuel characteristics. Acknowledging the inherently non-steady behavior of wildfire spread allows for more appropriate assessment and characterization of the hazard. Non-steady behavior is seen at a large scale due to natural wind fluctuations. However, recent studies have shown the importance of the intermittent behavior of the flame itself in the presence of steady wind. Interplay between buoyancy in the flame and the forced flow causes the intermittent flame behavior which impacts convective heating of fine fuels present in wildfires [7]. For example, intermittent flame bursts can cause extreme temperature variations that affect the ignition of fine fuels. Intermittent flame burst behavior has been studied using stationary burners under steady, perpendicular airflow to describe the movement and heating from the pulsations without flame spread [8]. The study characterized the downstream flame attachment fluctuation over time as demonstrated in Figure 2, which translates to intermittent flame contact to unburned fuel at a wildfire flame front.

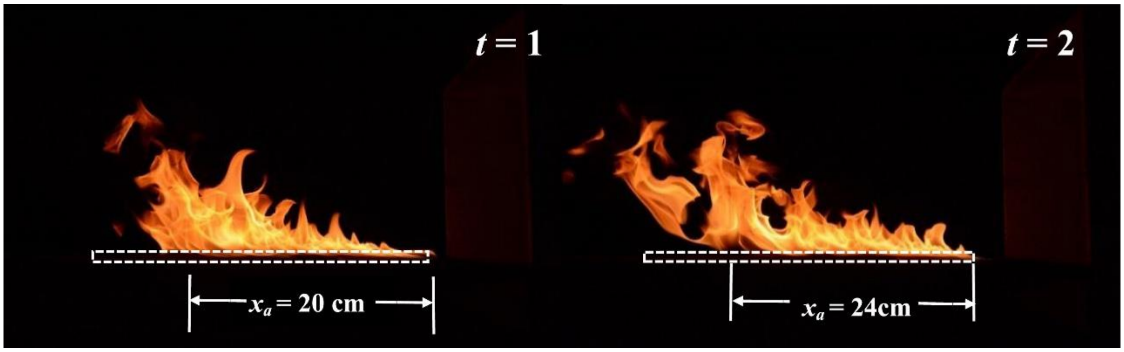

*Figure 2.* Flame attachment length ($x_a$) over two time steps in a forced flow experiment using a stationary burner, from Tang et.al [8].

Very few studies to date have characterized the flame spread rate response to changes in airflow. Albini used a heuristic based approach to characterize response to free-burning wildfires in non-steady wind conditions [9]. The model estimates a fire response considering various wildland fuels and observable billows of smoke, such as an acceleration or pausing spread at low frequency variations of less than 1/20 Hz. Mueller et.al. also studied the effects of non-steady wind in the wildfire setting, specifically how it impacts prescribed fires [10]. They performed field experiments with pine needle litter and measured the flame spread rate and the velocity of the light and gusty wind conditions. Non-steady fire behavior was observed due to the wind, including a hysteresis, or a lag in behavior, in the relationship between spread rate and wind velocity.

In addition, an experimental study was conducted by Zhu et.al. to analyze transitional behavior of flame spread under concurrent wind using PMMA [11]. The transition involved is a single step from a flame in still air to a steady velocity of concurrent flow. It was observed that once the flow was added to the flame, there was first a sharp increase to a peak spread rate, then the rate decreased and steadied to a constant. Lastly, a recent experimental study on the flame spread rate response to oscillating airflow in a horizontal configuration was performed by the author and her colleagues [12]. Under the concurrent flow conditions, the transient flame spread rate behavior did not present a clear oscillation response, but the heated length did have a clear oscillation. It was also determined that the airflow velocity amplitude was the greatest contributor to the transient response behaviors. These are the only studies to date researching the flame spread response to non-steady airflow.

## *1.1 Steady Opposed-Flow Flame spread*

In contrast, there is extensive research on downward flame spread under steady flow conditions. Flame spread occurs due to heat transfer from the flame to the fuel surface, and is highly dependent on the flame shape, or the gas flow conditions [13], [14]. For this reason, most studies are defined by the flow conditions (concurrent or opposed), and fuel orientation. Downward spread in opposed flow conditions is typically the slowest flame spread scenario; the flow pushes the flame downstream of the pyrolysis and reduces heat transfer to the unburned fuel. In one study, the effects of thin paper and thick PMMA were burned under varying opposed flow velocities and oxygen concentrations, as presented in Figure 3 below [15]. For both materials, an increase in oxygen concentration results in an increase in flame spread rate. When using air (approximately 23% mass fraction of oxygen ($Y_O$)) similar responses to the opposed flow velocity are seen. At low opposed flow velocities flame spread rate does not change significantly with increasing opposed flow velocity, but at larger opposed flow velocities, the flame spread rate decreases and eventually reaches a critical value beyond which extinction occurs[13]. Other ambient conditions that impact downward opposed flame spread are pressure and temperature. It was determined that flame spread rate decreases as ambient pressure decreases [4], [16], and as temperature decreases [17].

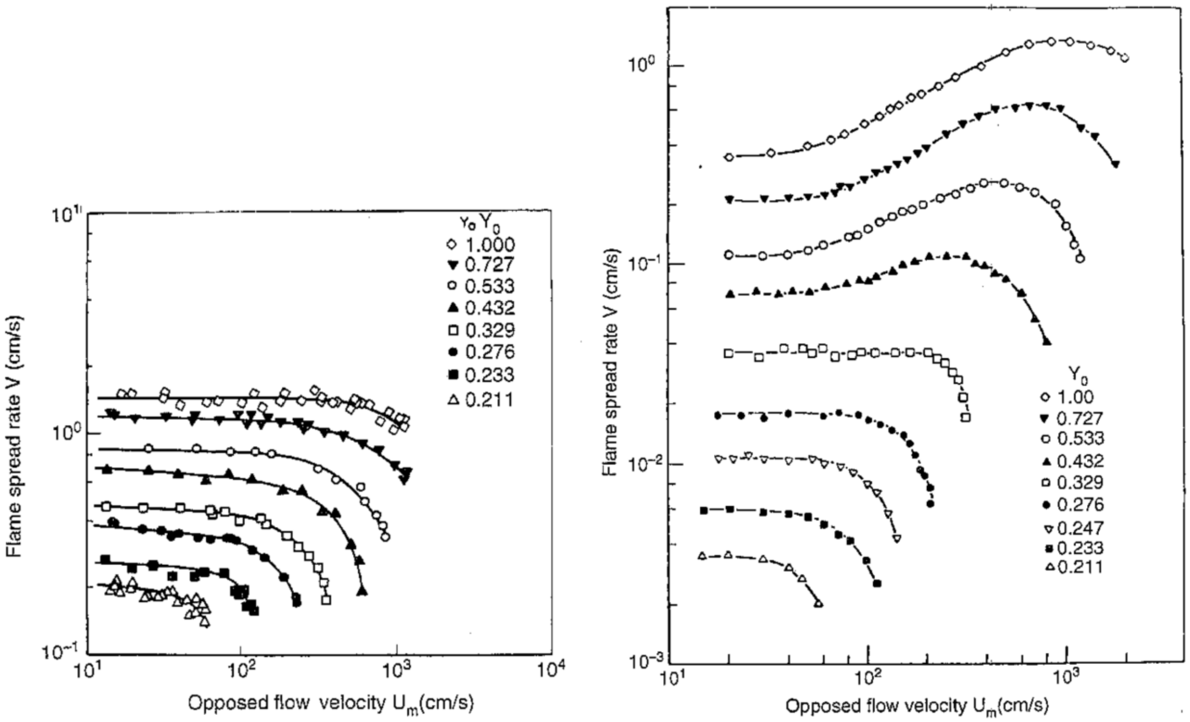

*Figure 3.* Effects of opposed flow velocity and oxygen concentrations on downward opposed flame spread of thin paper (left) and thick PMMA (right), from [15]. $Y_O$ is the mass fraction of oxygen.

De Ris developed a model for the spread of a flame on a thermally thin fuel against an opposed flow velocity. The thermally thin De Ris model is calculated using equation (1) below:

$$v_p = \frac{\sqrt{2}k_g\left(T_f - T_p\right)}{\rho_s c_{p,s}\left(T_p - T_\infty\right)\delta_s} \tag{1}$$

Where $v_p$ is the flame spread rate. A 'g' subscript denotes a gas phase property, and 's' denotes a solid phase. $T_f$ is the flame temperature, estimated to be 1400 K [18]. $T_p$ is the pyrolysis temperature of PMMA, 653 K [14], and $T_\infty$ is the ambient temperature, 298K. $\delta_s$ is the characteristic length of the solid. The PMMA is burning on both sides, therefore $\delta_s = \Delta x/2$. It is important to note that this solution does not consider the velocity of opposed airflow and how it interacts with the combustion reactions in the flame.

Another flame spread rate calculation model developed by Fernandez-Pello uses the Damkohler number, Da, to include the effects of opposed airflow velocity and blow off. The Damkohler number is a ratio of flow time to reaction time. At low Da numbers, the gases involved in the combustion reaction travel faster than the time required for a reaction to occur, leading to flame extinction or blow off. The Damkohler number is defined here using the equation below [13]:

$$\mathrm{Da} = \frac{A\Delta H_c \rho_g n W_O E Y_{O\infty} Y_{F,s}}{c_{p,g} R T_f^2 u_\infty / x} exp\left(-\frac{E}{RT_f}\right) \tag{2}$$

Where A is the pre-exponential factor in an Arrhenius equation, E is activation energy, n is the reaction order, and x is a coordinate parallel to the fuel surface. Subscript O denotes the oxidizer, and F denotes the fuel[1]. For a thermally thin material in the opposed flow configuration, Fernandez-Pello presents a flame spread rate calculation that is separated into two trends; equation (3) for high Da numbers and equation (4) for low Da numbers [13].

$$v_p = c\frac{\left(k_g \rho_g c_p\right)^{1/2}\left(T_f - T_p\right)}{\rho_s c_s \delta_s\left(T_p - T_\infty\right)} \tag{3}$$

$$v_p = \frac{c(u_\infty/x)^{1/2}}{ln(1 - \Gamma/Da)} \tag{4}$$

The expression for high Da numbers is very similar to the De Ris model in equation (1), and does not depend on the airflow velocity or reaction kinetics. Low Da numbers use a relationship between the Da number and Γ, the critical Damkohler number for ignition, which corresponds the point at which blow off will occur. In other words, extinction is predicted at Da = Γ. Figure 4 is a graph demonstrating the difference in trends between the two models discussed. This model has a similar constant spread rate calculation as the De Ris model at low opposed flow velocities, then decreases towards blow off as the airflow velocity increases. The Fernandez-Pello model can model the decreasing flame spread rate that is observed in experimental measurements as well as

---

[1] Remainder of the variables used are defined in Section 5, Nomenclature.

blow off (extinction), however the calculations are more complex that could make the Damkohler number unreasonable to use. For example, determining the chemical kinetics of the reaction (e.g., A and E) often requires a simplification of the gas phase combustion process as a 1-step global reaction that is not fully representative of the chemical process occurring for all possible conditions.

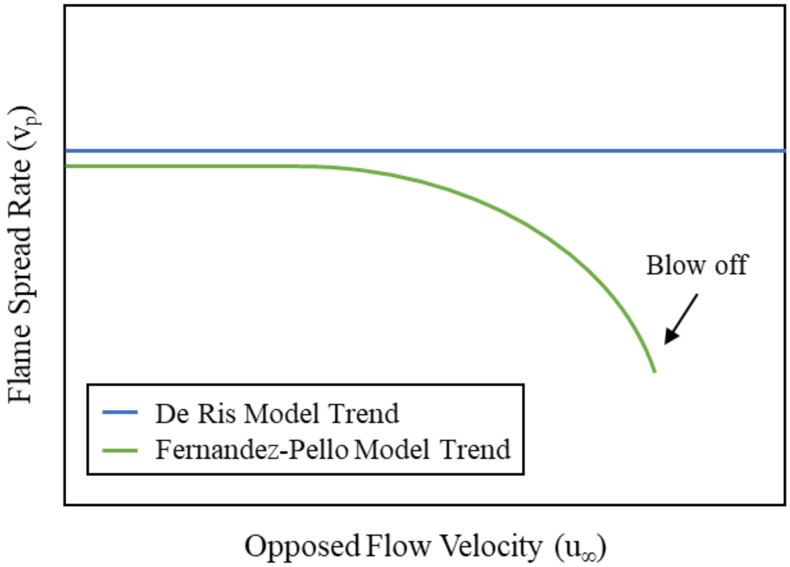

*Figure 4.* Approximate flame spread rate trends for the De Ris and Fernandez-Pello models for thermally thin material as opposed flow velocity changes.

The transient flame spread rate of downward spread under steady-state conditions has also been measured. In a study aiming to correlate burning rate and flame spread rate, the instantaneous downward flame spread rate of thick PMMA was recorded under steady ambient conditions, without forced flow [19]. In these transient measurements it was concluded that the flame spread rate was essentially constant throughout the entire experiment duration.

### *1.2 Scope of Present Work*

Understanding the impact of non-steady airflow on fire spread is important to describe the fire phenomena referenced in this section, yet there are very limited studies on this topic. The present study analyzes the response of non-steady, oscillating wind velocity on downward opposed flame spread of thin PMMA. The preliminary progress of this work was presented at 2024 spring technical meeting for the Eastern States Section of the Combustion Institute (ESSCI) [20].

## 2. Experimental Setup

Experiments were performed in a 1-meter-tall wind tunnel, as shown in Figure 5 and Figure 6. Compressed house air (and nitrogen purge) was controlled by a programmable mass flow controller (Aalborg DPC-77), and homogenized by marbles, honeycomb, and perforated sheets.

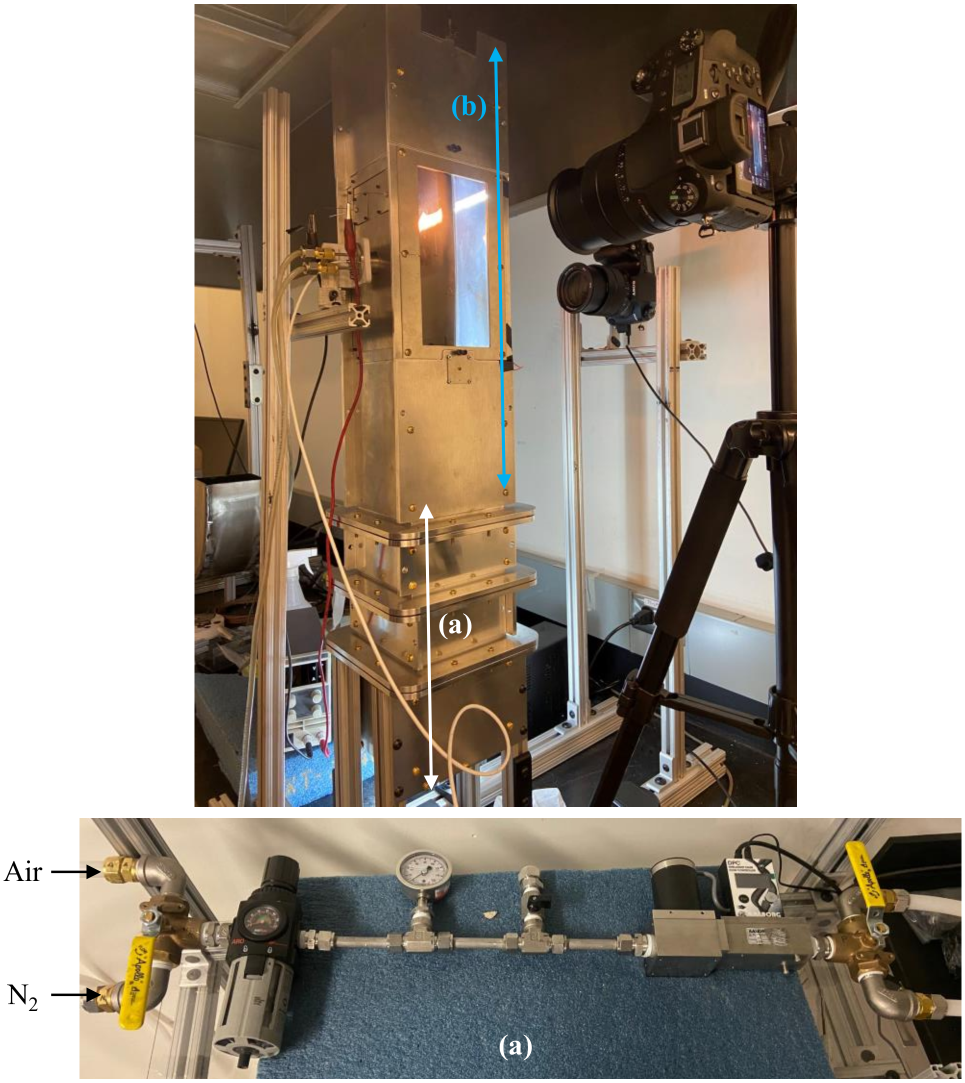

*Figure 5.* Images of the experimental set up, in which (a) labels the airflow supply (bottom pane) conditioning/straightening system (top pane), and (b) is the fuel experimental section of the tunnel.

The airflow was characterized by collecting a 3 by 4 by 5 array of measurement points within the sample section of the tunnel at seven different flows with a miniature wire probe anemometer. Air characterization results from the wind tunnel with an airflow of 250 SLPM are shown in Figure 7 below. The average variation in air speed over all tests is 4.6%, which confirmed uniform flow in the tunnel. A mass conservation balance was used to confirm the hot wire anemometer velocity measurements. Initial measurements found velocities greater than mass conservation laws permit, which can be accredited to high uncertainty in the device measurements at low velocities, as explained in Appendix A. The Dantec Dynamics-55P11 hot wire anemometer and Mini CTA 54T42 with an uncertainty of about 1% provided more reasonable results[2]. All mass flow controller measurements (in units of standard liters per minute (SLPM)) were converted to velocity using the

---

[2] Uncertainty is typically 1%, but depending on the calibration quality can increase to about 3%.

standard curve created with the Dantec Dynamics hot wire. Possible airflow speeds in the experimental section of the wind tunnel range from 0.0 – 0.65 m/s.

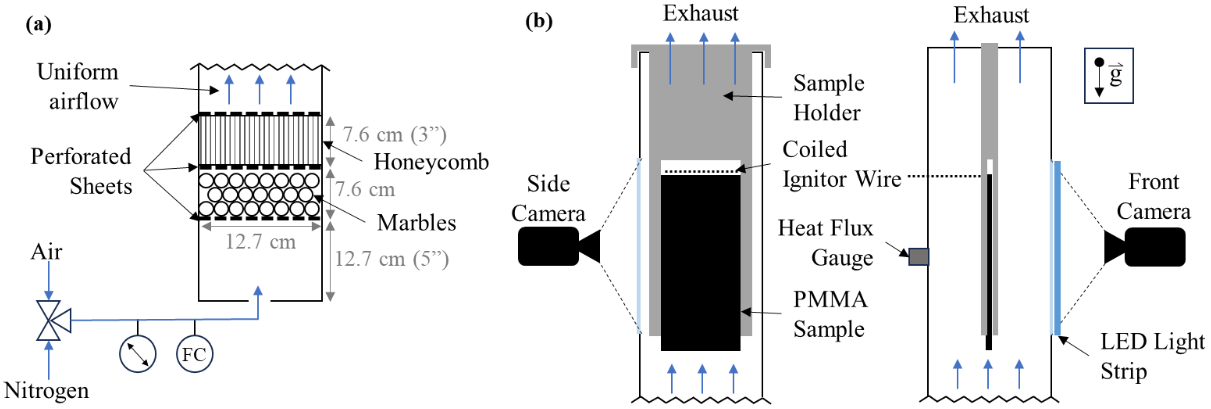

*Figure 6.* Experimental setup involving (a) the airflow input/straightening system and (b) the front and side views of the PMMA sample section in the wind tunnel respectively.

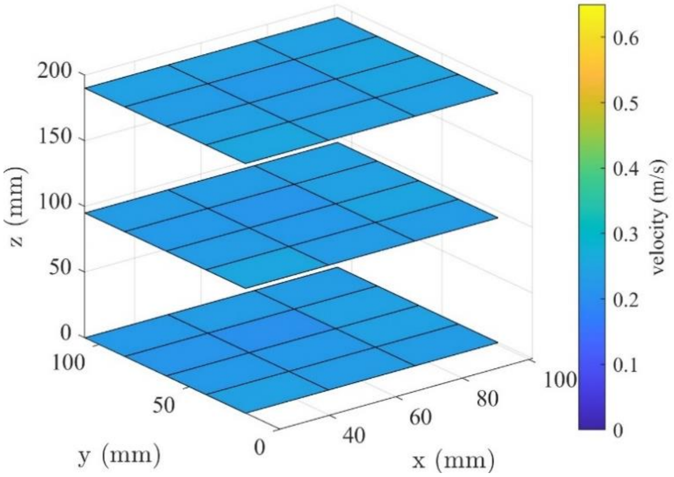

*Figure 7.* Airflow characterization measurements in the wind tunnel at 250 SLPM.

Each black-cast PMMA (Astra Products) fuel sample is 0.5 mm or 1 mm thin with the intent of producing thermally thin behavior and was 85 mm wide by 190 mm tall. A steel sample holder clamped the PMMA sample, as shown in Figure 8, and hung centered within the wind tunnel. The distance from the PMMA surface to the wind tunnel surface is approximately 6.35 cm (2.5"). A previous study by Zhu on the spacing effects of downward flame spread with 1mm thick PMMA found that this spacing will not impact the burning behavior or flame spread [21].

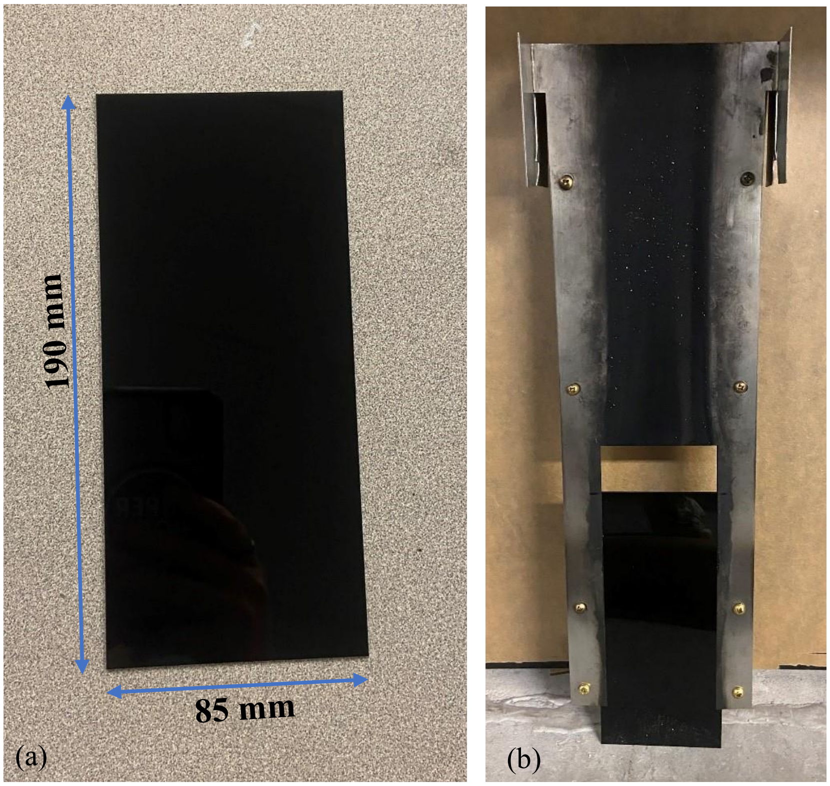

*Figure 8.* Image and measurements of the black-cast, glossy PMMA fuel (a) alone and (b) mounted within the sample holder.

A coiled 22AWG Nichrome 80 wire was used to ignite the sample from the top edge, and two cameras (Sony DSC-RX10M4) were used to record each experiment from the front and side faces of the PMMA. To make the location of the pyrolysis and burnout front location on the surface of the fuel clear, white LED strip lights framed the window (outside) facing the front PMMA. A heat flux gauge was used to measure the total heat flux from the flame, as depicted in Figure 5 and Figure 6. The gauge used was Huskeflux model SBG01, with a measurement range up to 5 kW/m$^2$. Due to the scope of this project, the results from the heat flux sensor are not presented but were collected for future project use.

For each experiment, the pyrolysis front location, $x_p$, burnout front location, $x_b$, and flame tip position, $x_f$, were recorded over time using an interactive MATLAB image processing script. Pyrolysis causes bubbling to occur on the fuel surface which is visible in the camera images with the illumination by the LED. The pyrolysis front, made visual by the LED strip lights, is defined by the presence of bubbling in the PMMA. When selecting a position, the maximum point in the downward direction where bubbling occurs is selected for $x_p$, and the maximum point in the upward direction where solid PMMA is present is selected for $x_b$, and the maximum point in the upward direction where a flame is present is selected for $x_f$. A diagram depicting each parameter recorded is shown in Figure 9.

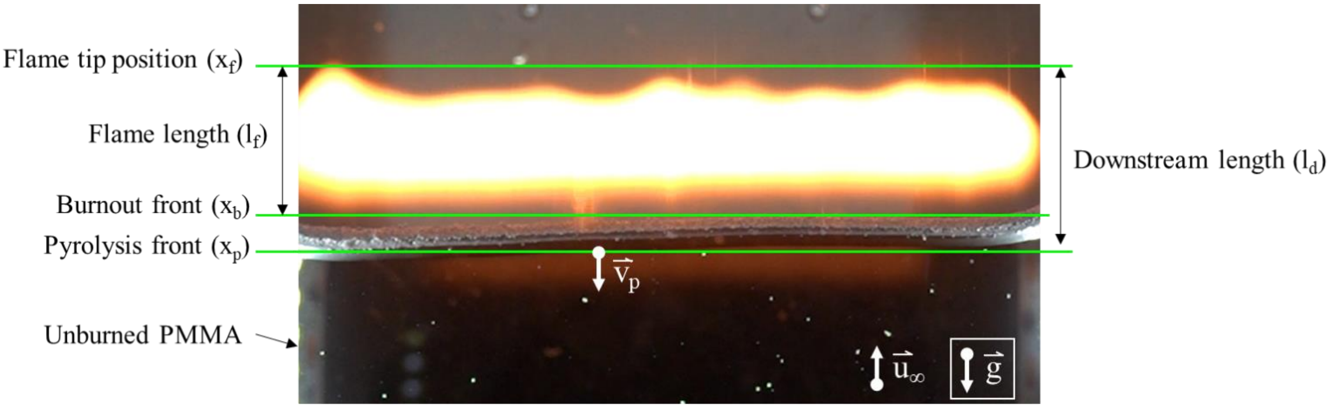

*Figure 9.* Visual demonstration of the pyrolysis front, $x_p$, burnout front, $x_b$, flame length, $l_f$, and flame tip position, $x_f$.

## *2.1 Experimental Conditions*

For each PMMA thickness, three steady airflow cases with five repetitions each were performed for air speeds 0.3, 0.45 and 0.6 m/s. The average flame spread rate, $\overline{v_p}$, was found by taking the average linear fit of the transient pyrolysis front data for each test. The slope of each repeat test is averaged together to calculate $\overline{v_p}$ at one steady flow.

Non-steady cases were also repeated five times, and their inlet flow velocities follow a sinusoidal curve, as demonstrated by Figure 10. All non-steady cases have a baseline velocity, $u_0$, of 0.45 m/s. Three frequencies, $f_{u\infty}$, of 1/8, 1/16, and 1/32 Hz, were used with three amplitudes, u', of 0.1, 0.15 and 0.2 m/s. PMMA was ignited under a steady flow rate, $u_0$, (baseline velocity with no oscillations) and once the ignitor coil no longer contacted the PMMA or the flame, a timer marked the start of the air oscillations and the beginning of data collection.

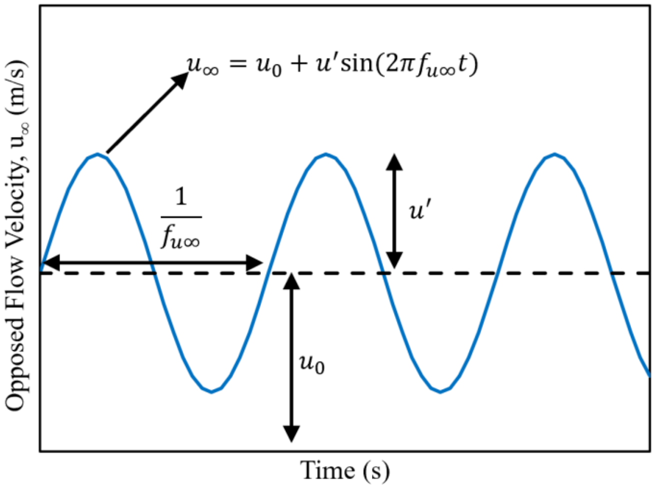

*Figure 10.* Non-steady airflow velocity curve.

To calculate transient flame spread rate, $v_p$, a Savitzky-Golay filter was applied to take the first derivative of $x_p$ data points over time. 32 data points were collected per period of air oscillation for 1/16 and 1/32 Hz frequencies. Therefore, the sample frequencies, $f_s$, were 2 and 1 Hz for $f_{u\infty}$ of 1/16 and 1/32 Hz respectively. The Savitzky-Golay window size for these data sets are 9 points, and a polynomial order of 2 was selected to fit the data. An example of how the Savitzky-Golay filter applied to the data is shown below.

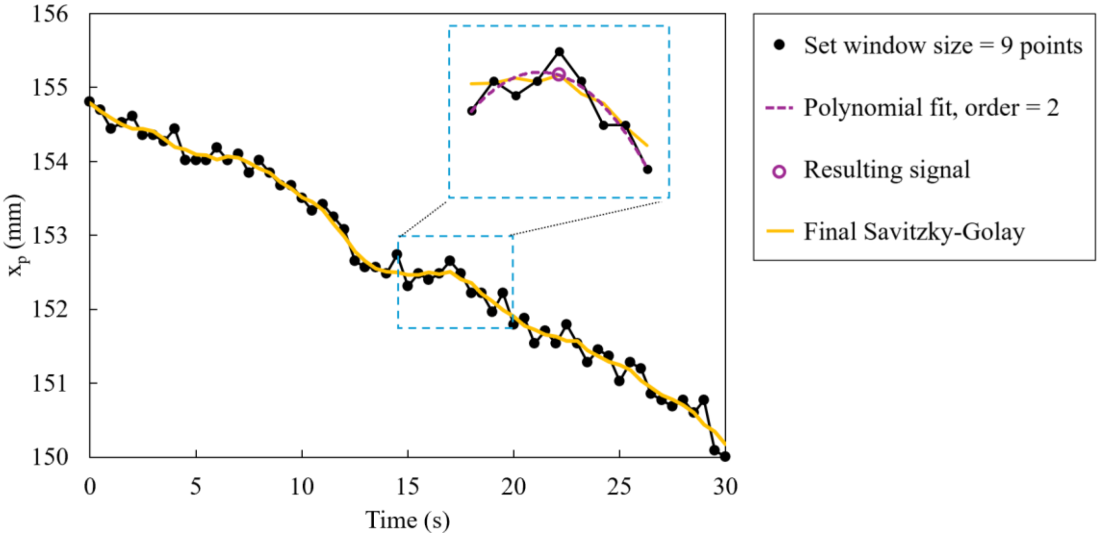

*Figure 11.* Savitzky-Golay filter demonstration for pyrolysis front over time. The flame spread rate, $v_p$, is calculated by taking the first derivative of the final Savitzky-Golay curve.

All sampling frequencies are greater than that required by the Nyquist theorem, which requires a sampling at least twice the airflow frequency ($f_s \geq 2f_{u\infty}$) [22]. To further verify the sampling frequencies, a test was performed on a dataset from each $f_{u\infty}$ to determine an adequate number of data points to collect per air velocity oscillation (i.e., one period). These tests are demonstrated in Appendix B. It was determined that more data points per oscillation period were required to appropriately represent the highest frequency (1/8 Hz) tests; 80 data points per oscillation ($f_s$ = 10 Hz) are required for 1/8 Hz airflow experiments. Table 1 summarizes the sample frequencies used for all experiments.

*Table 1.* Data collection frequency summary.

| Airflow Frequency ($f_{u\infty}$) | Data Sampling Frequency ($f_s$) | Points Collected per Period | Ratio of Savitzky-Golay Window to flow Period [-] |
|---|---|---|---|
| 1/8 Hz | 10 Hz | 80 | 0.263 |
| 1/16 Hz | 2 Hz | 32 | 0.281 |
| 1/32 Hz | 1 Hz | 32 | 0.281 |

# 3. Results and Discussion

## 3.1 Time Averaged Results

Steady airflow cases were performed for both thicknesses, and the time averaged flame spread rate, $\overline{v_p}$, was found using a least-squares trendline fit of $x_p$ over time. The results of these steady experiments are shown in Figure 12 below. A linear trend is observed for both thicknesses; as the airflow velocity increases, $\overline{v_p}$ decreases. In addition, as the PMMA thickness, Δx, increases, $\overline{v_p}$ decreases. From these initial results, it is confirmed that the flame spread rate is dependent on the opposed airflow. In addition, Figure 12 compares the measured values to the theoretical solution developed by De Ris (Equation (1)), for opposed flow flame spread on a thin surface [23], [24].

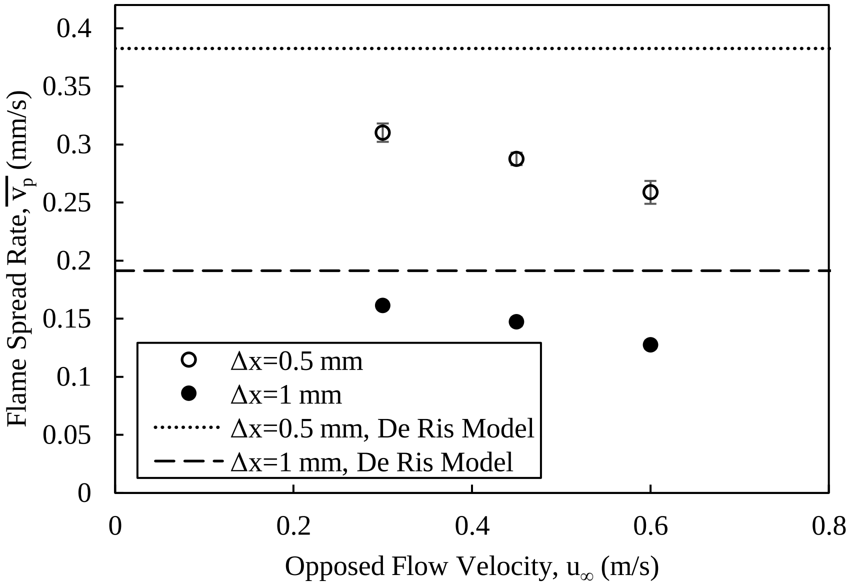

*Figure 12.* Average flame spread rate under various steady airflow conditions for both thicknesses of PMMA, and De Ris model comparisons. Error bars are ± the standard deviation between replicate tests. Note: error bars for Δx = 1mm cases are smaller than marker size.

The De Ris model does not predict the experimental trends observed because it does not account for reaction kinetics, or how the airflow speed impacts reaction kinetics [23]. Without these considerations, the De Ris model predicts spread rates about 20% larger than the experimental values with an opposed airflow of 0.3 m/s, and 50% larger than experimental values with an opposed airflow of 0.6 m/s and does not predict the trend with respect to the inlet flow speed. Based on these experimental results, the De Ris model loses accuracy with high opposed flow velocities, as the airflow speed reaches a similar timescale to the reaction speed. However, the simplicity of the model is beneficial and most appropriate to use at low airflow velocities.

The results from the steady airflow conditions were also compared to published experimental studies, such as those in Figure 3. The flame spread rates measured with both 0.5 and 1 mm PMMA are greater than reported thermally thick PMMA spread rates. All reported experimental trends have a decreasing flame spread rate with increasing opposed airflow velocity, however the linear decreasing slope has a greater magnitude for thinner materials (note that the figure presents flame spread rate on a logarithmic scale).

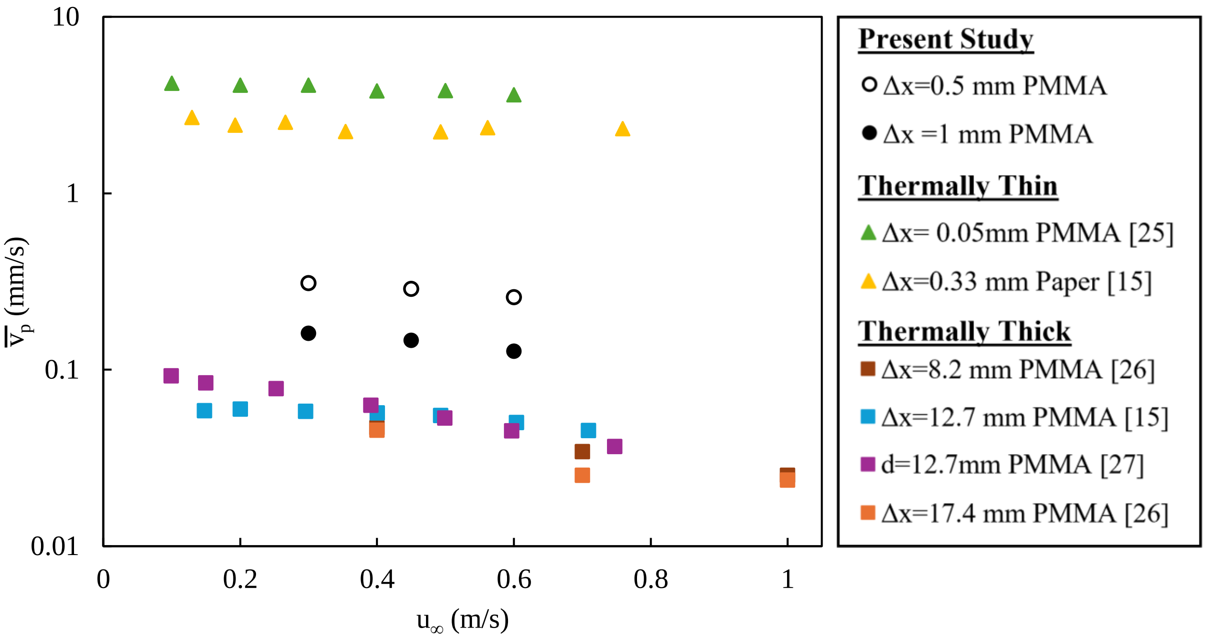

*Figure 13.* Experimental flame spread rates in comparison to published experimental studies with varying opposed airflow velocities [15], [25], [26], [27].

A time averaged spread rate was also determined for each non-steady airflow experiment. The average air velocity of all non-steady cases is equivalent to $u_0$ (0.45 m/s). In other words, where the airflow amplitude, u', is zero. Figure 14 presents the time averaged spread rate results for non-steady cases, and compares them to the $\overline{v_p}$ of a steady velocity of 0.45 m/s. For both PMMA thicknesses, all non-steady cases present a $\overline{v_p}$ that is approximately the same as a 0.45 m/s steady flow. Additionally, for the 1 mm thick PMMA, a slight trend may be seen due to airflow frequency; as airflow frequency, $f_{u\infty}$, increases, $\overline{v_p}$ decreases. However, these effects are very minimal, and further investigation is needed to confirm this phenomenon.

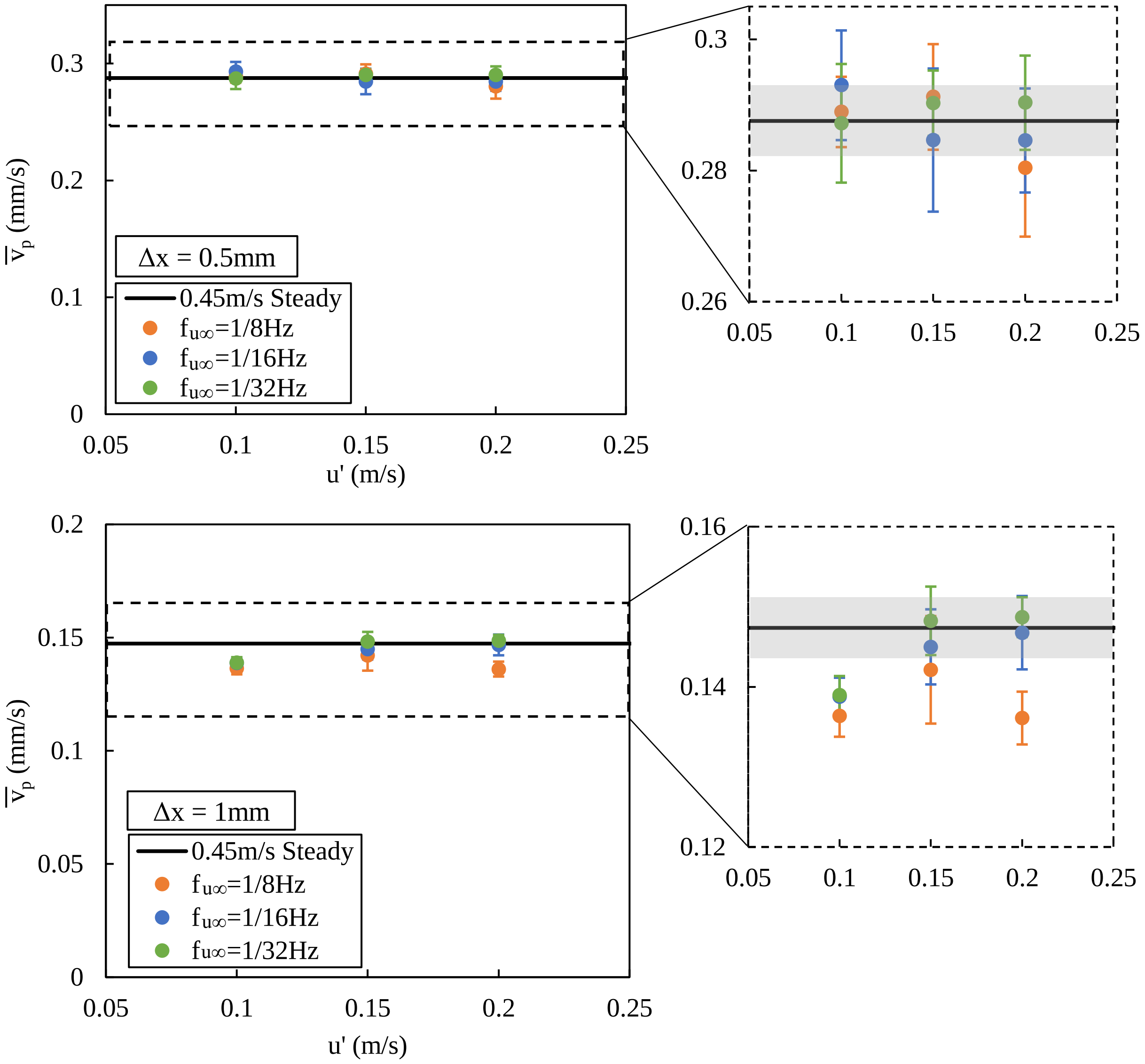

*Figure 14.* Time averaged flame spread rate in non-steady flow cases as a function of airflow velocity amplitude. The straight black line is the spread rate for $u_\infty$ = 0.45 m/s, and shaded region represents its error bars. Error bars are ± the standard deviation between replicate tests.

It is important to acknowledge that the flow conditions of these experiments contain both forced flow and buoyancy induced flow. At these steady flow cases, an initial characterization of the mixed convection conditions was done using the Richardson number, Ri. This parameter has been used in many previous studies because it presents a ratio of the buoyancy to opposed flow using the Grashof number, Gr, and Reynolds number, Re [8], [28], [29], [30]. The Richardson number is calculated using the following equation:

$$Ri = \frac{Gr}{Re^2} = \frac{g\beta\left(T_f - T_\infty\right)l_d}{u_\infty^2} \tag{5}$$

Where g is the acceleration due to gravity and $l_d$ is the downstream distance along the plate, which was calculated as the distance between the pyrolysis front, $x_p$, and the flame tip position, $x_f$. The coefficient of the volumetric expansion, β, is considered to be $1/T_f$, and $T_f$ is estimated to be 1400 K [18]. Ri can be used to classify the controlling convection force using the following three regimes: [29]

$$Ri = \begin{cases} < 0.1 & \text{forced convection controlled} \\ 0.1 \sim 10 & \text{mixed convection} \\ > 10 & \text{natural convection controlled} \end{cases} \tag{6}$$

First considering the steady flow, $u_\infty$ is a constant, and the average distance $l_d$ for each steady case was used to calculate the results in Table 2. Based on these calculations and the regime definitions above, all steady flow cases are under mixed convection.

*Table 2.* Calculated Richardson number for each steady flow case.

| **Δx** | **$u_\infty$ = 0.3 m/s** | **$u_\infty$ = 0.45 m/s** | **$u_\infty$ = 0.6 m/s** |
|---|---|---|---|
| 0.5 mm | 1.88 ±0.09 | 0.64 ±0.03 | 0.25 ±0.01 |
| 1 mm | 1.90 ±0.06 | 0.63 ±0.01 | 0.26 ±0.02 |

### *3.2 Transient Results*

The transient flame spread rate, $v_p$, was calculated using a Savitzky-Golay filter of $x_p$ over time. Example results from individual repetitions are shown in Figure 15. From initial observations of these graphs, a response in $v_p$ could be observed. While clearer in the lower frequencies, as the airflow increases the instantaneous $v_p$ often decreases. However, the amount of noise in the individual results seems to increase with $f_{u\infty}$.

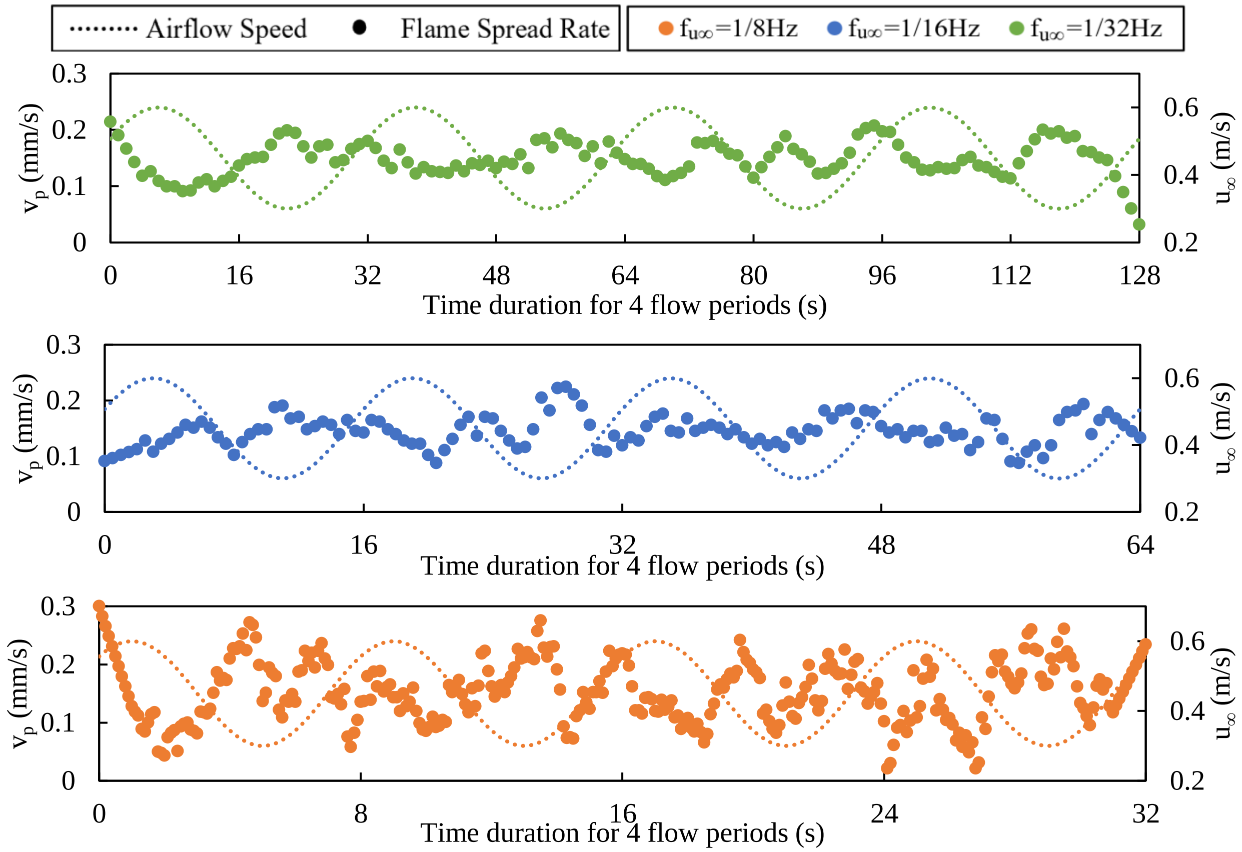

*Figure 15.* Transient flame spread rate and air velocity over time from an example test for Δx = 1 mm, and u' = 0.15 m/s. Note that each x-axis represents the time for 4 airflow velocity periods which changes with the flow frequency.

While experiments such as the 1/8 Hz frequency test shown in Figure 15 don't have an obvious oscillating trend, the instantaneous spread rate is still varying within the time of the experiment. Investigating this further, the maximum change in instantaneous spread rate, $\Delta v_p$, was calculated over the duration of each experiment including 4 oscillation periods ($\max(v_p) - \min(v_p)$). The transient flame spread rate for the steady state experiments were calculated to serve as a baseline for this analysis. Figure 16 confirms that all non-steady cases have some level of response to the airflow change, as each maximum $\Delta v_p$ is greater than the steady flow experiments. It also demonstrates that the variation in $v_p$ increases as the airflow frequency increases.

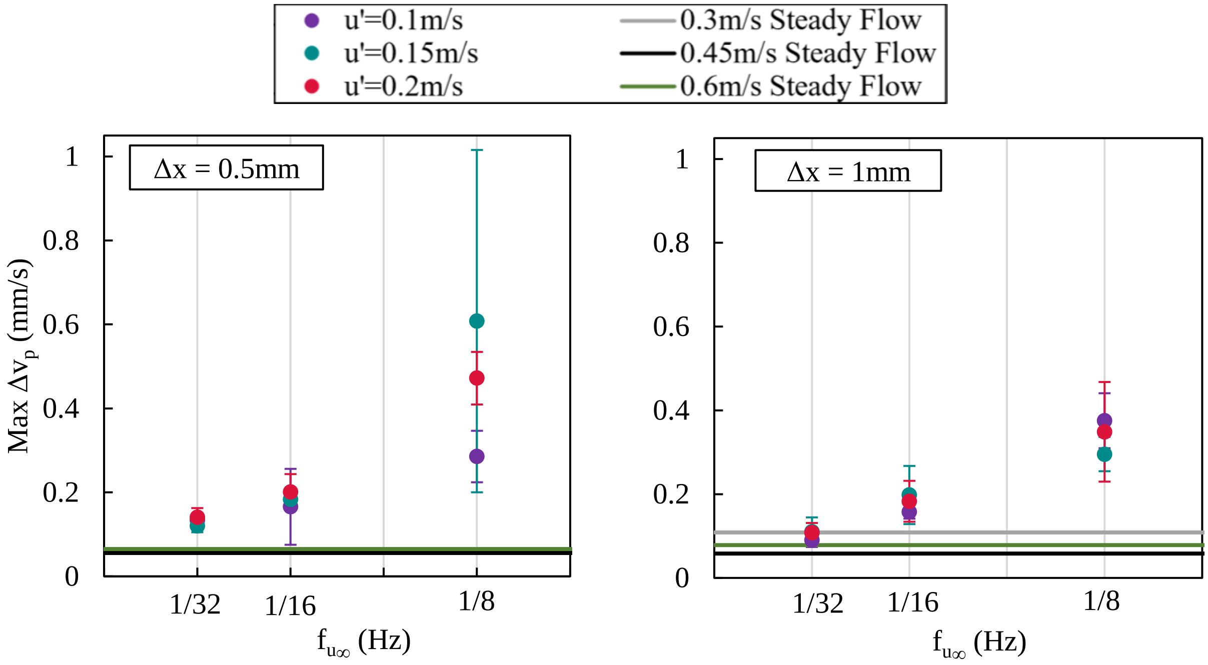

*Figure 16.* The maximum change in instantaneous spread rate, max $\Delta v_p$, over the test duration for each non-steady case, in comparison to the max $\Delta v_p$ for steady flow cases ($f_{u\infty} = 0$). Error bars are ± the standard deviation between replicate tests.

To demonstrate the instantaneous increase in flame spread rate when an oscillating airflow impacts the flame, Figure 17 shows the ratio of the maximum measured $v_p$ to the average $\overline{v_p}$ at 0.45 m/s. Again, no trend is seen based on the amplitudes used in these experiments, but the maximum increase in instantaneous flame spread rate is seen at the highest frequency, 1/8 Hz. An increase in the instantaneous flame spread rate of up to about 126% in comparison to the time-averaged flame spread rate is observed.

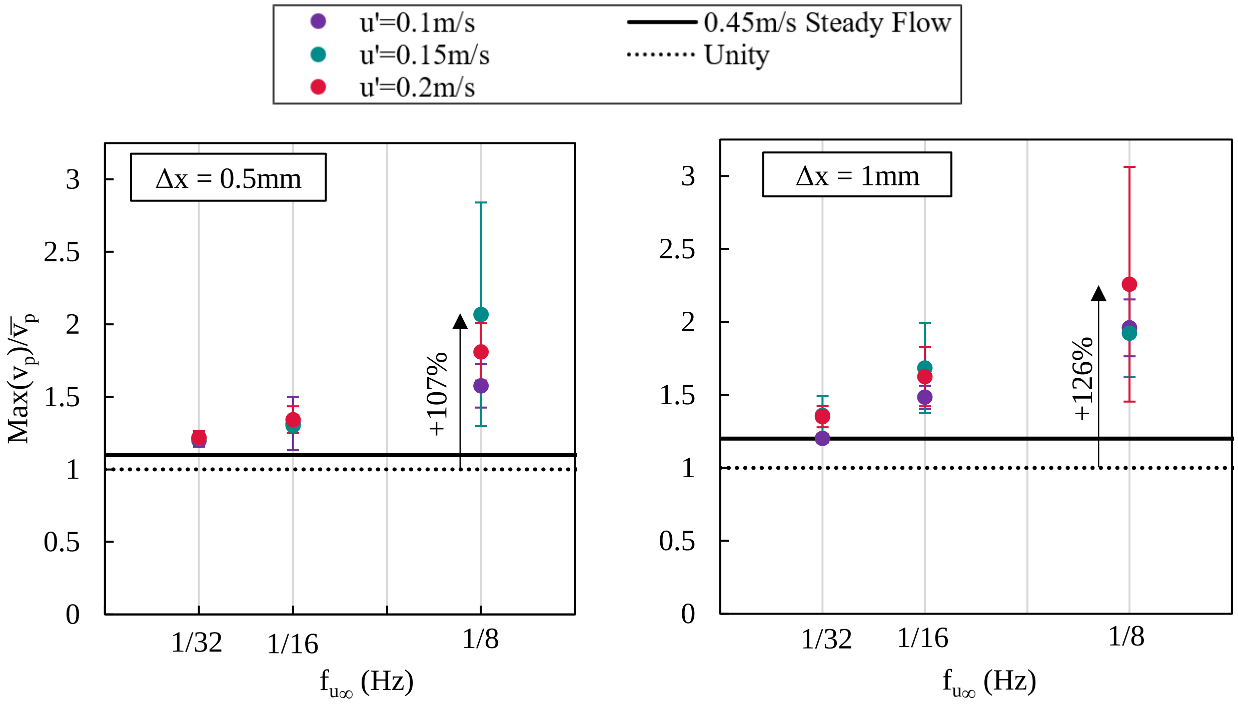

*Figure 17*. The ratio of the maximum measured instantaneous flame spread rate to the average flame spread rate for 0.45 m/s steady flow. Error bars are ± one standard deviation between replicate tests. Solid lines represent the maximum $v_p$ of a steady flow condition over the time averaged spread rate.

Considering the mixed convection occurring in these experiments, the transient $l_d$ and $u_\infty$ were used to calculate the Richardson number for all non-steady cases. These results are graphed in Figure 18. All Richardson numbers are within 0.1 to 10, and therefore are under the mixed convection regime.

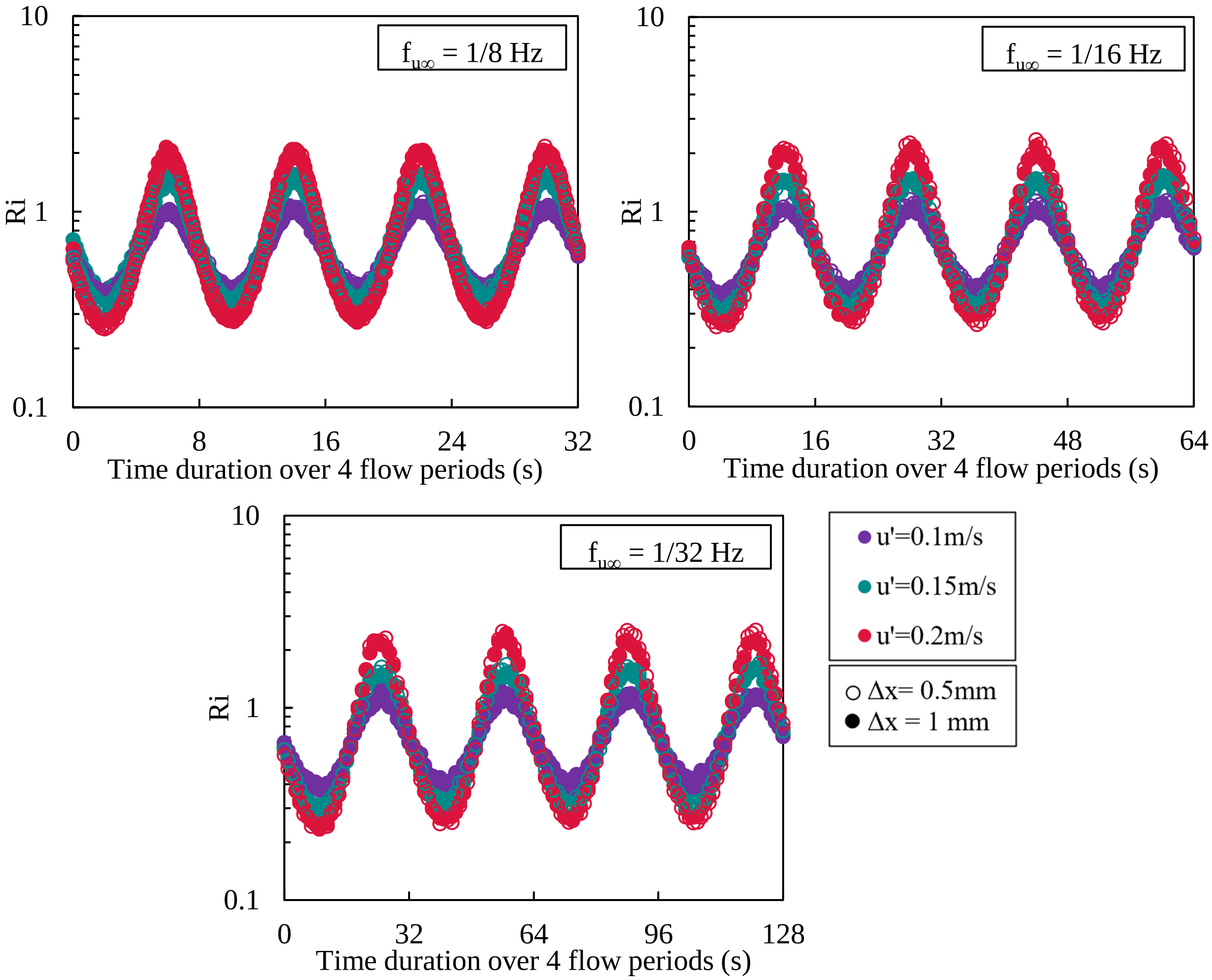

*Figure 18.* Richardson number over time for all non-steady conditions.

### *3.3 Fourier Transform Analysis*

A goal of this project is to analyze results in a quantitative method, rather than using visual observations which can be vague and unclear. Fast Fourier transform (FFT) calculations can be used to quantitatively determine whether a frequency response is occurring in the flame behavior. An FFT confirms the presence of a frequency when a peak is observed in the spectrum, and the amplitude of the peak corresponds to the signal strength from the oscillations. Figure 19 shows the FFT results from the transient $v_p$ data. Calculations were performed on individual tests, which were then averaged together. The FFT frequency spectrum is presented as a ratio of FFT frequency to opposed airflow frequency; the ratio is equal to 1 at airflow frequency, $f_{u\infty}$.

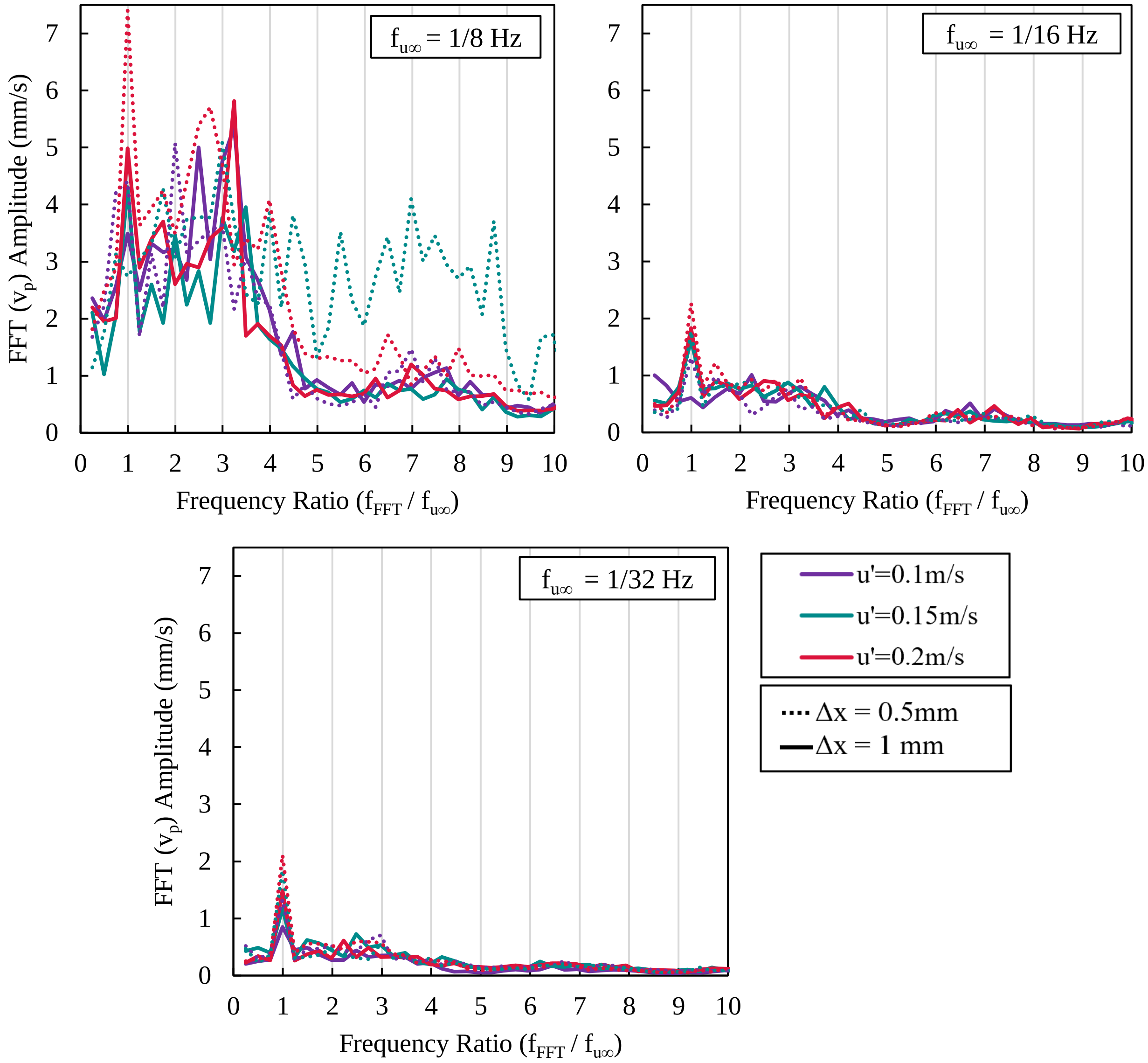

*Figure 19.* Averaged Fast Fourier Transform results on transient flame spread rates for all non-steady test conditions. The FFT frequency is normalized by the opposed airflow frequency.

For both low frequencies tested, 1/16 and 1/32 Hz, a very clear peak is formed in the FFT spectrum of most tests at the frequency of the forced airflow, and no other significant peaks are observed. In other words, there is a transient response in $v_p$ due to the opposed airflow with the same frequency. However, the same response is not seen for the highest airflow frequency, 1/8 Hz[3].

To further analyze the extent of the transient $v_p$ response, the magnitude of the FFT amplitude at the opposed airflow frequency is graphed in Figure 20. For all cases except for 0.5 mm thin

---

[3] An FFT analysis was also performed on the steady state cases to confirm no $v_p$ frequencies were observed in these cases. The results are shown in Appendix C.

PMMA with a 1/8 Hz airflow, an increasing linear trend in FFT response as u’ increases. In addition, the FFT response is greater for the thinner PMMA in each flow condition.

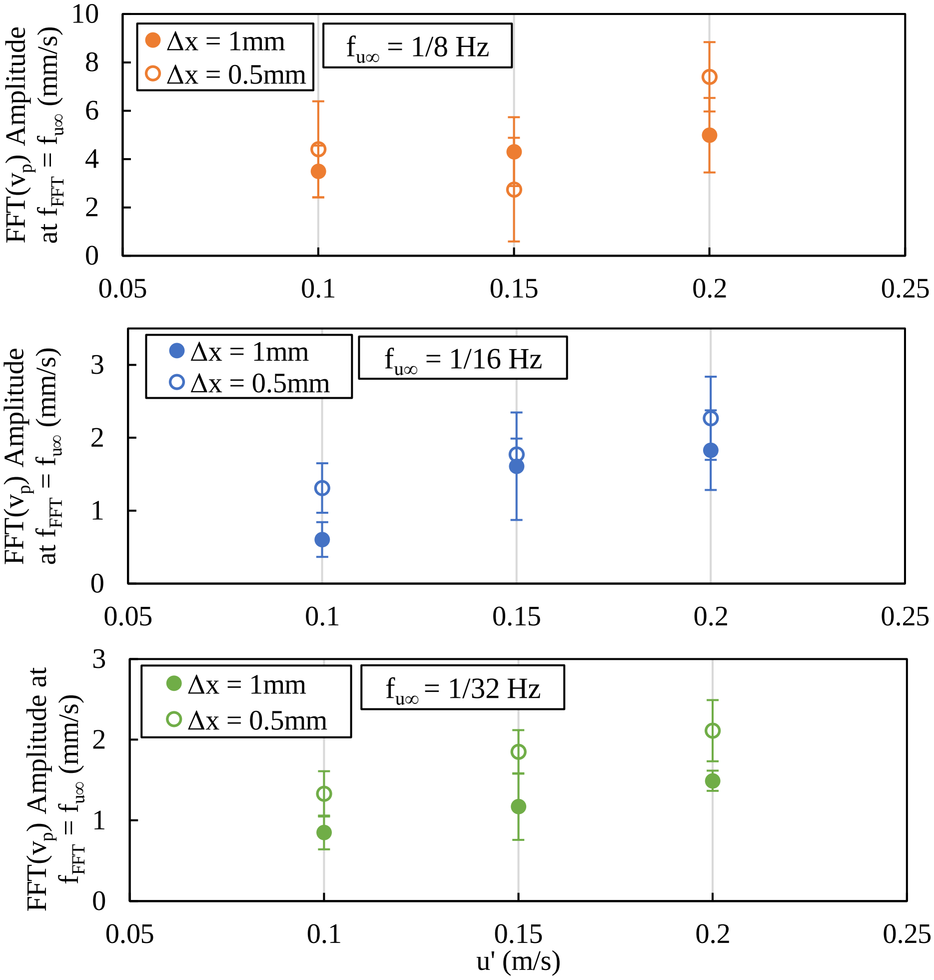

*Figure 20.* Magnitude of $v_p$ FFT amplitude at the opposed airflow velocity. Error bars are ± the standard deviation between replicate tests.

The same FFT analysis was performed on the temporal evolution of flame length ($l_f = x_f - x_b$), as shown in Figure 21 and Figure 22. The response of $l_f$ is very clear in all airflow conditions with no other significant peaks, including the higher frequency of 1/8 Hz. When analyzing the magnitude of FFT amplitude for $l_f$ at the forced flow frequency, the same increasing linear trend in FFT amplitude is seen as u’ increases, and there is a greater amplitude for the thinner PMMA.

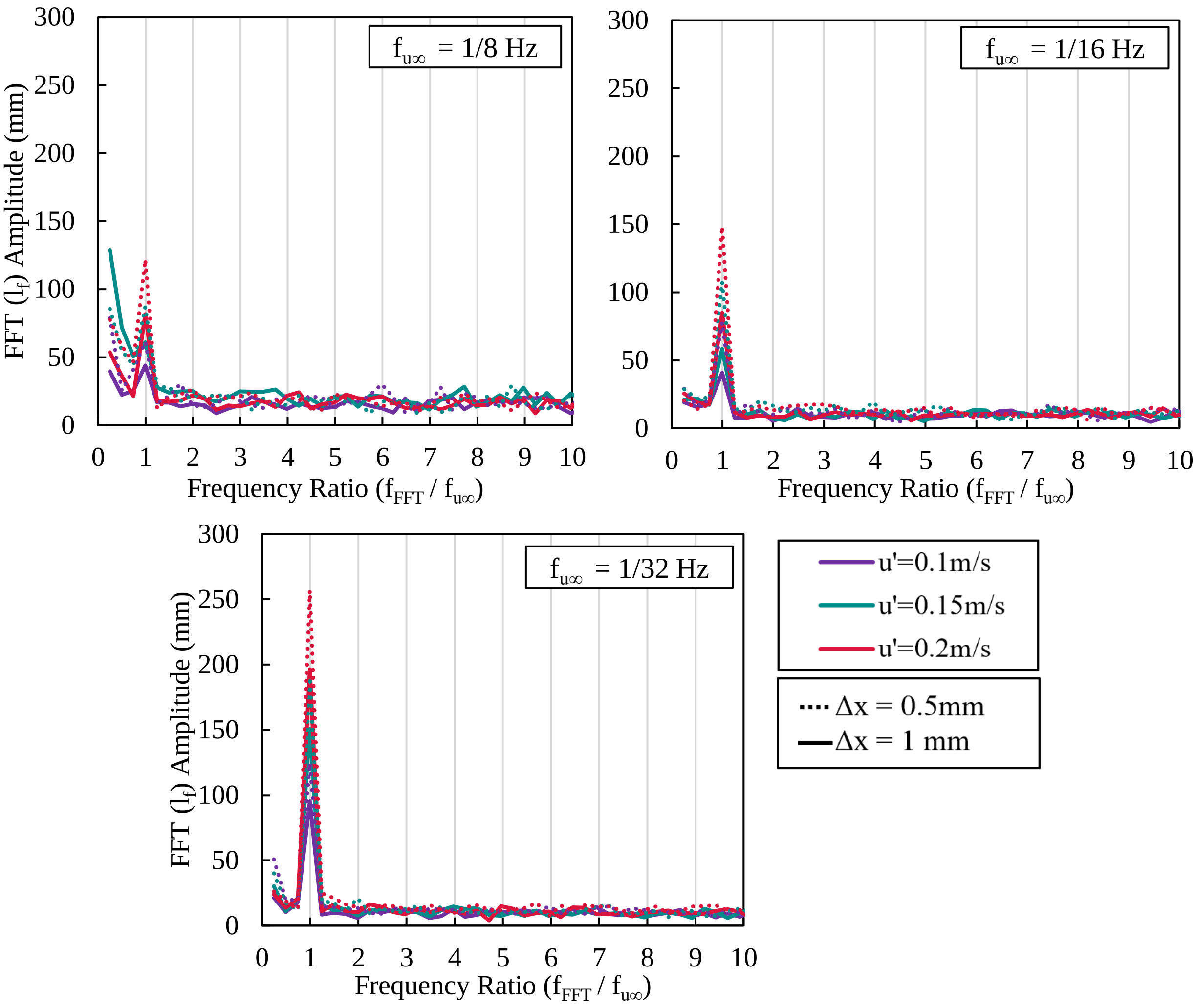

*Figure 21.* Averaged Fast Fourier Transform results on transient flame length for all non-steady test conditions. The FFT frequency is normalized by the opposed airflow frequency.

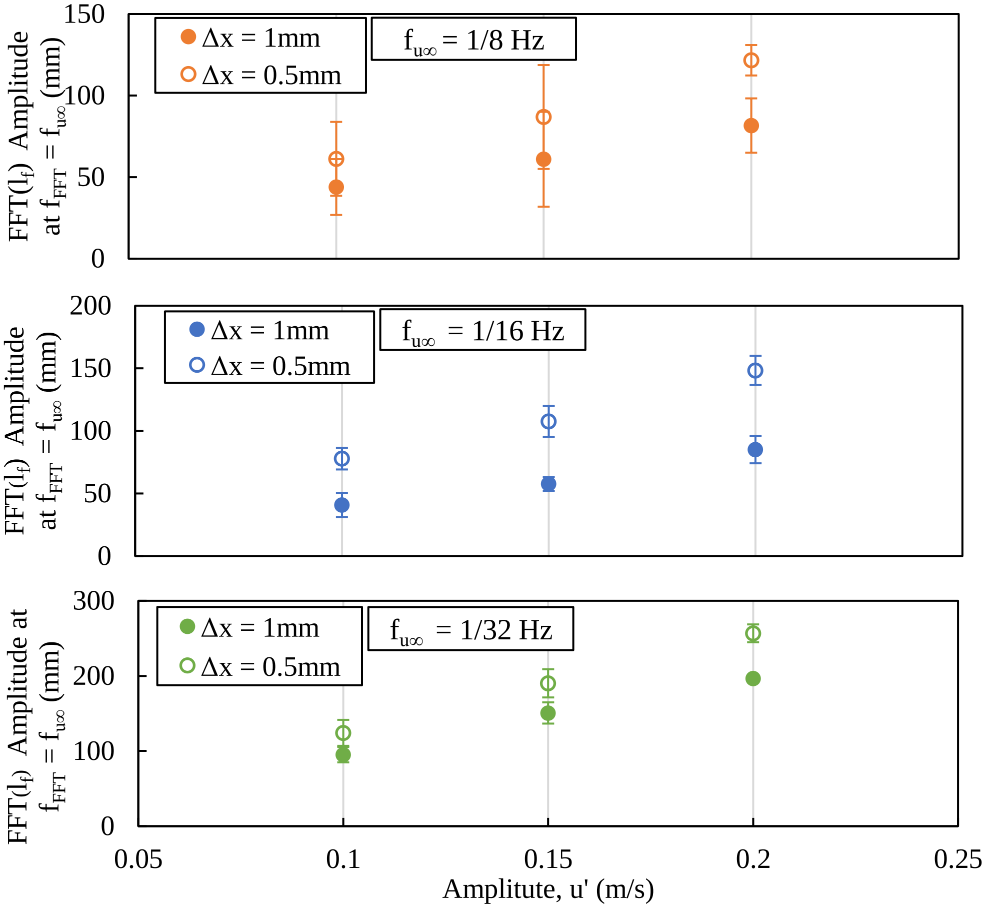

*Figure 22.* Magnitude of $l_f$ FFT amplitude at all opposed airflow conditions. Error bars are ± the standard deviation between replicate tests.

The FFT analysis of transient $v_p$ and $l_f$ demonstrates the difference in gas- and solid- phase response time. The gas phase response is fast enough to respond in the 1/8 Hz flow frequency, but the solid phase is not. To investigate the solid phase response further, the approximate ignition time can be used to characterize the solid phase response time using equation (7) which is derived from the expression $v_p \approx l_h/t_{ig}$ [14].

$$t_{ig} \approx \frac{l_h}{\overline{v_p}} \tag{7}$$

Where $l_h$ is the heated length, and $\overline{v_p}$ is the average flame spread rate, taken from the experimental steady flow rate results at 0.45 m/s. Heated length was not directly measured as a part of this experiment, however the length is estimated to be 2 mm based on previous experimental studies by Fernandez-Pello et al. [31] and Ito et al. [32]. The results of the ignition time calculations are given in Table 3.

*Table 3.* Calculated ignition times for each PMMA thickness, for $u_\infty = 0.45$m/s.

| **Δx (mm)** | **$\overline{v_p}$ (mm/s)** | **$t_{ig}$ (s)** |
|---|---|---|
| 0.5 | 0.2876 ±0.0053 | 6.955 ±0.128 |
| 1 | 0.1474 ±0.0037 | 13.57 ±0.34 |

It is predicted that a solid phase response will be observed only when $t_{ig}$ is shorter than the time it takes for a significant change in the airflow. The time between the most significant changes in airflow is estimated to be half of the oscillation period, P. For an oscillating airflow pattern, the change from decreasing to increasing velocity occurs over half of the period length, as demonstrated by Figure 23, which is the most significant velocity change. In other words, if the solid phase can respond to a decreasing velocity before it changes to an increasing trend, it is expected that an oscillating response will be observed in the flame spread rate.

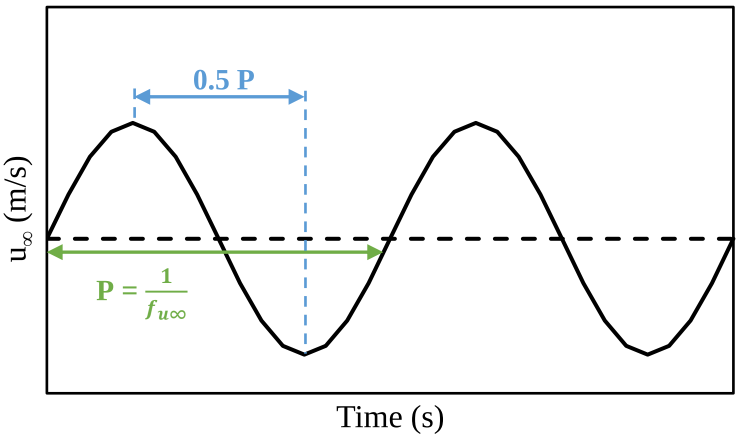

*Figure 23.* A full airflow oscillation period, P, and half of the period demonstrated as the change from increasing to decreasing velocity.

A ratio of the estimated ignition time to the period, $t_{ig}/P$, is used in Figure 24, to determine if this prediction is correct. The ratio is compared to a binary response for if a clear individual peak is seen in the FFT results at $f_{FFT}$ equal to $f_{u\infty}$. A "clear individual peak" is present where there is an increase in FFT amplitude is observed above the surrounding frequencies. As $t_{ig}/P$ decreases, FFT peaks are present at the airflow frequency. A transition point was predicted to be present at a critical value of $t_{ig}/P$, close to 0.5 in magnitude, which would correspond to when the ignition time is half of the period. A transition point at a critical value is observed; however, the transition is present at a $t_{ig}/P$ of approximately 0.86. Therefore, it is estimated that a solid phase response to oscillating airflow is present when the ignition time is less than 86% of the airflow oscillation period.

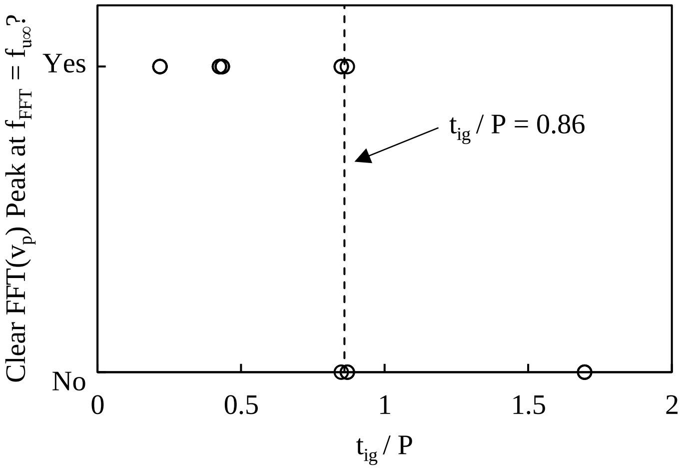

*Figure 24.* Ratio of the approximate ignition time to the oscillation period, $t_{ig}/P$, for each test condition, and if there was a clear individual peak in flame spread rate FFT at $f_{FFT} = f_{u\infty}$.

A few factors could contribute to the difference between the prediction and result of the $t_{ig}$ analysis. For example, a time averaged flame spread rate was used to calculate the approximate ignition time, rather than transient flame spread rates. It is concluded from experimental data that $\overline{v_p}$ for oscillating airflow is approximately equal to the spread rate at the average airflow velocity. However, the instantaneous spread rate variations found within that experiment time may play an important role. In addition, the heated length, which is largely dependent on gas-phase impacts, was not measured in this experiment and may have important transient impacts.

# 4. Conclusion

An experimental study of the flame spread rate response to non-steady airflow was conducted in a downward, opposed flame spread configuration. Thin black-cast PMMA was burned in a vertical wind tunnel under steady and oscillating airflow velocities. Oscillating velocity conditions included 3 frequencies and 3 amplitudes. Using a Richardson number analysis, all airflow conditions are classified under a mixed convection regime. The time averaged flame spread rate for non-steady airflow was found to be approximately equal to the spread rate at the average airflow velocity. However, a response in instantaneous flame spread rate was observed for all cases. $v_p$ changes over time in all non-steady conditions, and the maximum $\Delta v_p$ increases as $f_{u\infty}$ increases. For 0.5 and 1 mm thick PMMA, a high airflow frequency of 1/8 Hz causes the instantaneous flame spread rate to increase up to an additional 107% and 126% of the average airflow spread rate, respectively.

FFT analysis was used to determine the signal strength at the frequency of the forced flow. Flame length has a strong FFT response at $f_{u\infty}$ in all non-steady cases, demonstrating an instantaneous response to airflow changes in the gas phase. The FFT amplitude value increases with u’ and $\Delta x$. Flame spread rate has a FFT response at $f_{u\infty}$ in most cases, however the signal is less clear at higher frequencies. A characteristic time in the solid was estimated as a hypothetical ignition time for the preheat zone. This characteristic time was used to investigate solid phase response. Based on FFT peak observations, it is estimated that an instantaneous flame spread rate response can be recorded when ignition time is less than 86% of the oscillation period.

# 5. Nomenclature

| | | |
|---|---|---|
| A | Pre-exponential factor for Arrhenius expression | [1/s] |
| c | Generic constant | [-] |
| d | Diameter | [mm] |
| Da | Damkohler number | [-] |
| E | Activation energy | [J/mol] |
| $f_s$ | Data sampling frequency | [Hz] |
| $f_{u\infty}$ | Airflow frequency | [Hz] |
| $f_{FFT}$ | FFT frequency | [Hz] |
| g | Gravity | 9.81 [m/s] |
| Gr | Grashof number | [-] |
| $\Delta H_c$ | Heat of combustion | [J/kg] |
| k | Thermal conductivity | [W/mK] |
| $l_d$ | Downstream distance ($x_f - x_p$) | [mm] |
| $l_f$ | Flame length | [mm] |
| $l_h$ | Heated length | [mm] |
| $l_p$ | Pyrolysis length | [mm] |
| P | Oscillation period | [s] |
| Re | Reynolds number | [-] |
| Ri | Richardson number | [-] |
| t | Time | [s] |
| $T_f$ | Flame temperature | [K] |
| $t_{ig}$ | Approximate ignition time | [s] |
| $T_p$ | Pyrolysis temperature | [K] |
| $T_\infty$ | Ambient temperature | [K] |
| u | Velocity | [m/s] |
| u' | Airflow velocity amplitude | [m/s] |
| $u_0$ | Initial velocity | [m/s] |
| $u_\infty$ | Wind tunnel velocity | [m/s] |
| $v_p$ | Instantaneous flame spread rate | [mm/s] |
| $\overline{v_p}$ | Time averaged flame spread rate | [mm/s] |
| W | Molecular weight | [g/mol] |
| x | Coordinate parallel to fuel surface | [m] |
| $x_b$ | Burnout front position | [mm] |
| $x_f$ | Flame tip position | [mm] |

|  |  |  |
|---|---|---|
| $x_p$ | Pyrolysis front position | [mm] |
| $\Delta x$ | PMMA thickness | [mm] |
| $Y_i$ | Mass faction of species i | [kg/kg] |
| $\beta$ | Coefficient of volume expansion | [1/K] |
| $\delta$ | Characteristic length | [m] |
| $\Gamma$ | Critical Damkohler number for ignition | [-] |

## 6. References

[1] R. A. Altenkirch and M. Vedha-Nayagam, “Opposed-flow flame spread and extinction in mixed-convection boundary layers,” Symposium (International) on Combustion, vol. 22, no. 1, pp. 1495–1500, Jan. 1989, doi: 10.1016/S0082-0784(89)80159-6.

[2] F. Zhu, Z. Lu, and S. Wang, “Flame Spread and Extinction Over a Thick Solid Fuel in Low-Velocity Opposed and Concurrent Flows,” Microgravity Sci Technol, vol. 28, no. 2, pp. 87–94, May 2016, doi: 10.1007/s12217-015-9475-4.

[3] A. C. Fernandez-Pello, S. R. Ray, and I. Glassman, “Flame spread in an opposed forced flow: the effect of ambient oxygen concentration,” Symposium (International) on Combustion, vol. 18, no. 1, pp. 579–589, Jan. 1981, doi: 10.1016/S0082-0784(81)80063-X.

[4] M. Thomsen, C. Fernandez-Pello, S. L. Olson, and P. V. Ferkul, “Downward burning of PMMA cylinders: The effect of pressure and oxygen,” in Proceedings of the Combustion Institute, Elsevier Ltd, 2021, pp. 4837–4844. doi: 10.1016/j.proci.2020.05.024.

[5] K. Zhao, M. J. Gollner, Q. Liu, J. Gong, and L. Yang, “Lateral Flame Spread over PMMA Under Forced Air Flow,” Fire Technol, vol. 56, no. 2, pp. 801–820, Mar. 2020, doi: 10.1007/s10694-019-00904-x.

[6] E. Guillaume, V. Dréan, B. Girardin, F. Benameur, and T. Fateh, “Reconstruction of Grenfell Tower fire. Part 1: Lessons from observations and determination of work hypotheses,” Fire Mater, vol. 44, no. 1, pp. 3–14, Jan. 2020, doi: 10.1002/fam.2766.

[7] M. A. Finney et al., “Role of buoyant flame dynamics in wildfire spread,” Proceedings of the National Academy of Sciences, vol. 112, no. 32, pp. 9833–9838, Aug. 2015, doi: 10.1073/pnas.1504498112.

[8] W. Tang et al., “An experimental study on the intermittent extension of flames in wind-driven fires,” Fire Saf J, vol. 91, pp. 742–748, Jul. 2017, doi: 10.1016/J.FIRESAF.2017.03.030.

[9] F. A. Alblni, “Response of Free-Burning Fires to Nonsteady Wind,” Combustion Science and Technology, vol. 29, no. 3–6, pp. 225–241, Dec. 1982, doi: 10.1080/00102208208923599.

[10] E. Mueller et al., “Flame spread and combustion dynamics in pine litter under unsteady wind conditions.,” in Advances in Forest Fire Research 2022, Imprensa da Universidade de Coimbra, 2022, pp. 1469–1474.

[11] N. Zhu, X. Huang, J. Fang, L. Yang, and L. Hu, “Transitional flame-spread and fuel-regression behaviors under the change of concurrent wind,” Fire Saf J, vol. 120, p. 103015, Mar. 2021, doi: 10.1016/J.FIRESAF.2020.103015.

[12] P. Pinto, X. Xi, A. Miska, M. Thomsen, and J. Urban, “Transient horizontal flame spread under non-steady concurrent airflow.,” Fire Saf J, 2024.

[13] A. Fernandez-Pello, “The Solid Phase,” in Combustion Fundamentals of Fire, G. Cox, Ed., San Diego: Academic Press, 1995, pp. 34–96.

[14] J. G. Quintiere, Fundamentals of fire phenomena. John Wiley, 2006.

[15] A. C. Fernandez-Pello, S. R. Ray, and I. Glassman, “Flame spread in an opposed forced flow: the effect of ambient oxygen concentration,” Symposium (International) on Combustion, vol. 18, no. 1, pp. 579–589, Jan. 1981, doi: 10.1016/S0082-0784(81)80063-X.

[16] M. Thomsen, C. Fernandez-Pello, X. Huang, S. Olson, and P. Ferkul, “Buoyancy Effect on Downward Flame Spread Over PMMA Cylinders,” Fire Technol, vol. 56, no. 1, pp. 247–269, Jan. 2020, doi: 10.1007/s10694-019-00866-0.

[17] K. K. Wu, W. F. Fan, C. H. Chen, T. M. Liou, and I. J. Pan, “Downward flame spread over a thick PMMA slab in an opposed flow environment: experiment and modeling,” Combust Flame, vol. 132, no. 4, pp. 697–707, Mar. 2003, doi: 10.1016/S0010-2180(02)00520-5.

[18] Dougal. Drysdale, “Heat transfer,” in An introduction to fire dynamics, vol. 3rd Edition, Wiley, 2011, pp. 35–82.

[19] L. Carmignani, B. Rhoades, and S. Bhattacharjee, “Correlation of Burning Rate with Spread Rate for Downward Flame Spread Over PMMA,” Fire Technol, vol. 54, no. 3, pp. 613–624, May 2018, doi: 10.1007/s10694-017-0698-3.

[20] A. Miska, P. Pinto, X. Xi, and J. Urban, “Downward opposed flame spread response to non-steady airflow,” in Spring Technical Meeting of the Eastern States Section of the Combustion Institute, 2024.

[21] H. Zhu, Y. Gao, R. Pan, and B. Zhong, “Spacing effects on downward flame spread over thin PMMA slabs,” Case Studies in Thermal Engineering, vol. 13, p. 100370, Mar. 2019, doi: 10.1016/J.CSITE.2018.100370.

[22] H. J. Landau, “Sampling, data transmission, and the Nyquist rate,” Proceedings of the IEEE, vol. 55, no. 10, pp. 1701–1706, 1967, doi: 10.1109/PROC.1967.5962.

[23] J. N. De Ris, “Spread of a laminar diffusion flame,” Symposium (International) on Combustion, vol. 12, no. 1, pp. 241–252, Jan. 1969, doi: 10.1016/S0082-0784(69)80407-8.

[24] A. S. Rangwala and V. Raghavan, “Burning of Solids,” in Mechanism of Fires, 1st ed., Cham: Springer International Publishing, 2022, pp. 115–152. doi: 10.1007/978-3-030-75498-3.

[25] S. Bhattacharjee, M. Laue, L. Carmignani, P. Ferkul, and S. Olson, “Opposed-flow flame spread: A comparison of microgravity and normal gravity experiments to establish the thermal regime,” Fire Saf J, vol. 79, pp. 111–118, Jan. 2016, doi: 10.1016/J.FIRESAF.2015.11.011.

[26] K. K. Wu, W. F. Fan, C. H. Chen, T. M. Liou, and I. J. Pan, “Downward flame spread over a thick PMMA slab in an opposed flow environment: experiment and modeling,” Combust Flame, vol. 132, no. 4, pp. 697–707, Mar. 2003, doi: 10.1016/S0010-2180(02)00520-5.

[27] S. Link, X. Huang, C. Fernandez-Pello, S. Olson, and P. Ferkul, “The Effect of Gravity on Flame Spread over PMMA Cylinders,” Sci Rep, vol. 8, no. 1, p. 120, Jan. 2018, doi: 10.1038/s41598-017-18398-4.

[28] C.-P. Mao, A. C. Fernandez-Pello, and P. J. Pagni, “Mixed Convective Burning of a Fuel Surface With Arbitrary Inclination,” 1984. [Online]. Available: http://asmedigitalcollection.asme.org/heattransfer/article-pdf/106/2/304/5526795/304_1.pdf

[29] Y. Zhang, W. Zhang, Y. Lin, Y. Chen, and K. Li, “Flame attachment effect on the distributions of flow, temperature and heat flux of inclined fire plume,” Int J Heat Mass Transf, vol. 174, p. 121313, Aug. 2021, doi: 10.1016/J.IJHEATMASSTRANSFER.2021.121313.

[30] M. J. Gollner, C. H. Miller, W. Tang, and A. V. Singh, “The effect of flow and geometry on concurrent flame spread,” Fire Saf J, vol. 91, pp. 68–78, Jul. 2017, doi: 10.1016/J.FIRESAF.2017.05.007.

[31] A. C. Fernandez-Pello and R. J. Santoro, “On the dominant mode of heat transfer in downward flame spread,” Symposium (International) on Combustion, vol. 17, no. 1, pp. 1201–1209, Jan. 1979, doi: 10.1016/S0082-0784(79)80114-9.

[32] A. Ito and T. Kashiwagi, “Characterization of flame spread over PMMA using holographic interferometry sample orientation effects,” Combust Flame, vol. 71, no. 2, pp. 189–204, Feb. 1988, doi: 10.1016/0010-2180(88)90007-7.

# 7. Appendices

## *Appendix A. Airflow characterization*

Below are the graphed results from all the airflow characterization tests, which confirm that the airflow through the wind tunnel within the sample holder region is homogeneous.

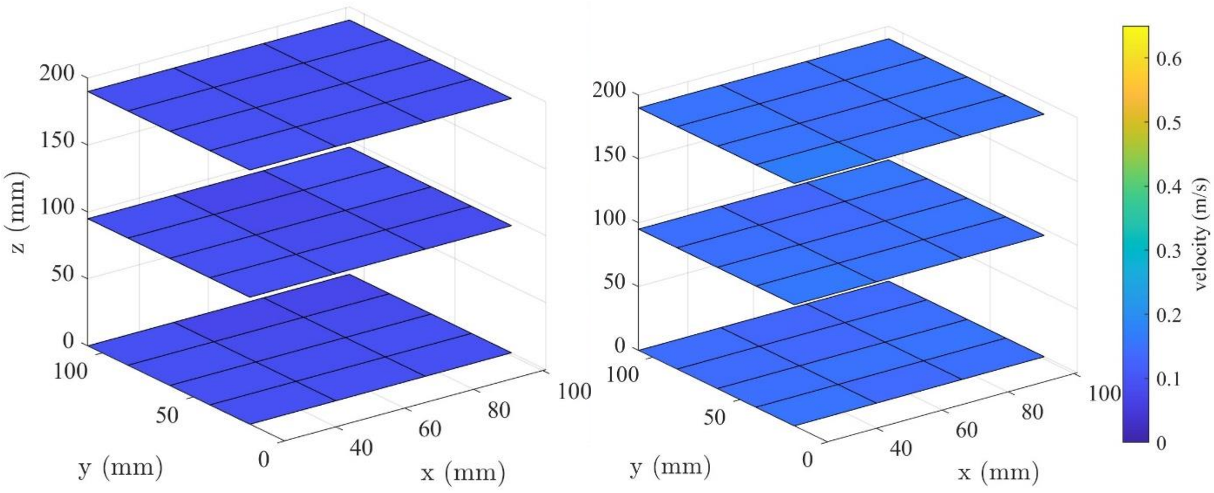

*Figure 25.* Airflow characterization results at 100 SLPM (left) and 150 SLPM (right).

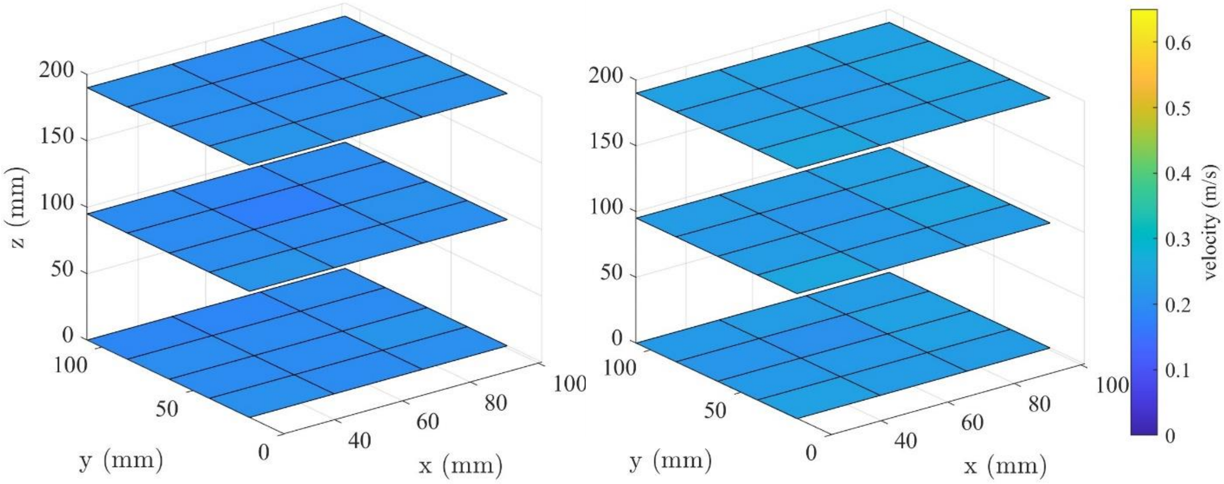

*Figure 26.* Airflow characterization results at 200 SLPM (left) and 250 SLPM (right).

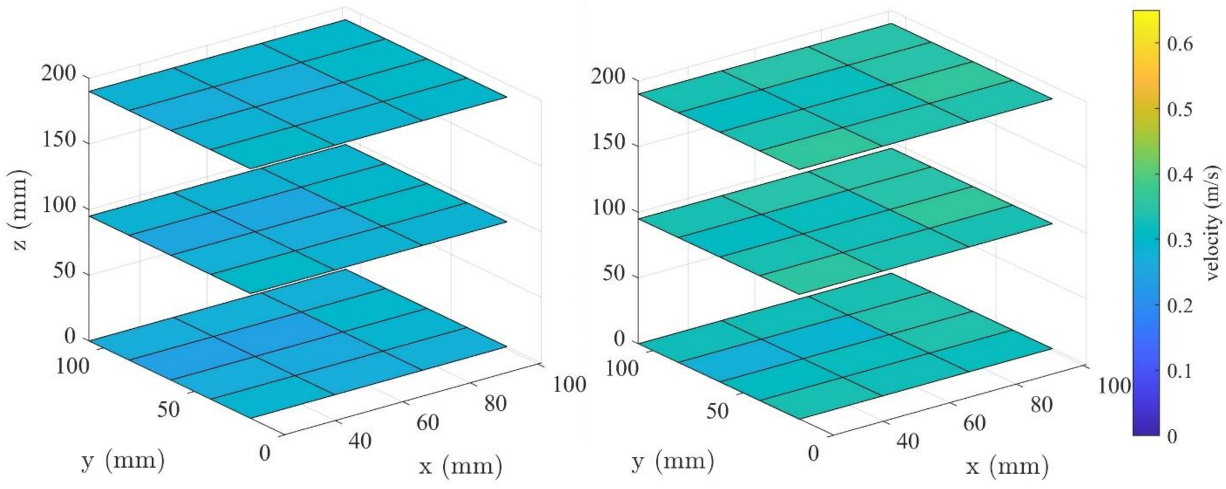

*Figure 27.* Airflow characterization results at 300 SLPM (left) and 350 SLPM (right).

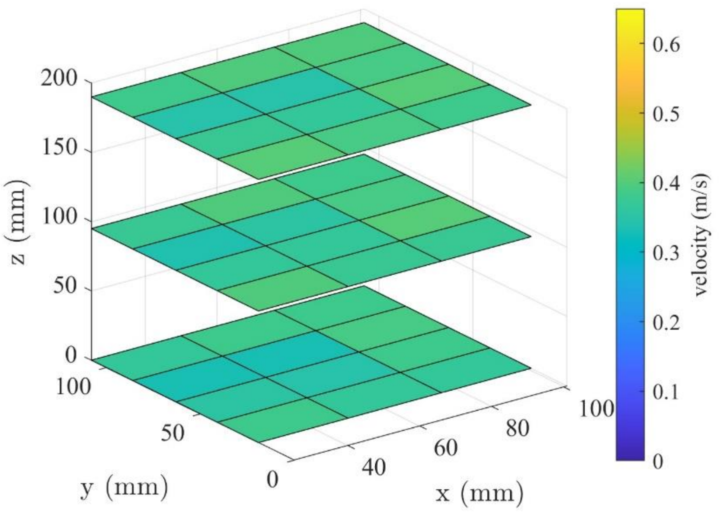

*Figure 28.* Airflow characterization results at 400 SLPM.

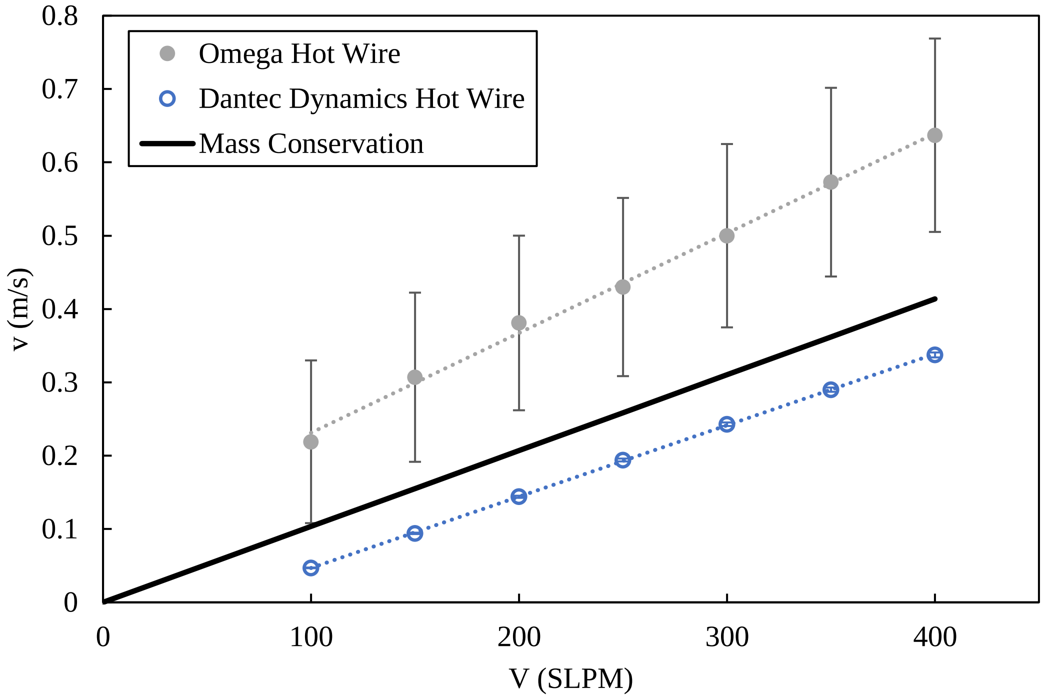

*Figure 29.* Difference in velocity measurements between Dantec and Omega hot wire anemometer. The solid black line is the calculated velocity due to complete mass conservation. Error bars represent measurement device uncertainty.

During preliminary airflow characterization tests, a large error in mass conservation was found (shown in Figure 29 above), which lead to an important discovery regarding the uncertainty of the Omega hot wire anemometer (HHF-SD1 model) device at low velocities. Online, the measurement accuracy is listed as ±5%, working down to a velocity of 0.2 m/s. However, in the physical manual provided after purchasing the device, specifications state that the airspeed measurement accuracy is ±5% + 0.1 m/s. At the low air speeds measured in this experiment, that is a significant difference in accuracy and is believed to be the cause of the mass conservation error. For that reason, other hot wire anemometers were tested, and final calculations were performed based on the Dantec Dynamics hot wire and Mini CTA 54T42, with a 1-3% accuracy.

## *Appendix B. Savitzky-Golay data collection resolution*

The graphs below are example cases in which the necessary quantity of data collection points per experiment was determined. For each airflow frequency, a test case was taken in which multiple data collection frequencies were used to calculate $v_p$. The data collection point quantities were selected at the lowest frequency at which no important $v_p$ behavior was missed. When calculating $v_p$, the time length of the window size remained constant.

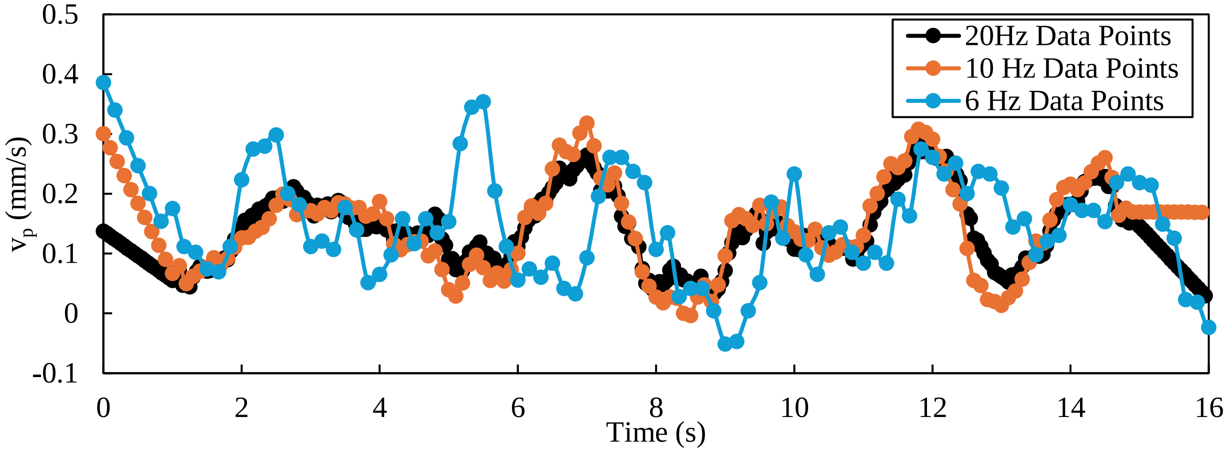

*Figure 30.* Flame spread results comparison between various data point collection resolutions for 1/8Hz airflow, 1mm PMMA thickness and an amplitude of 0.15m/s. Selected resolution is 10Hz.

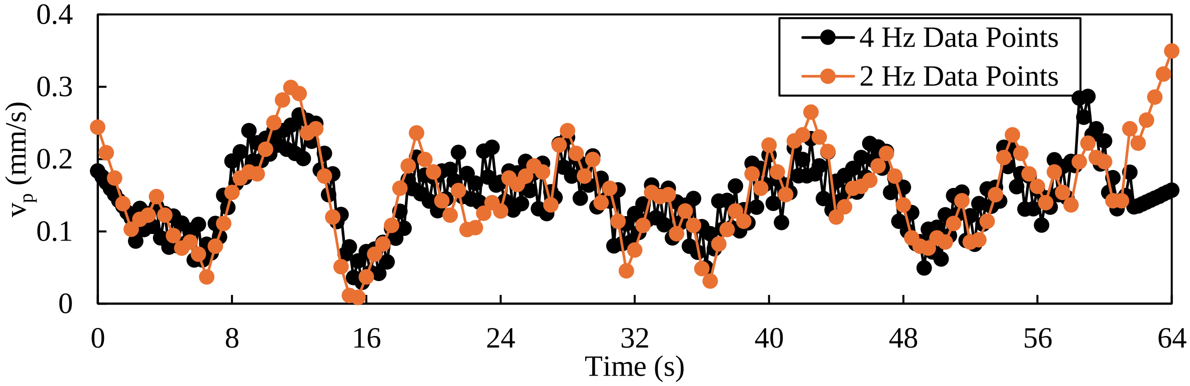

*Figure 31.* Flame spread results comparison between various data point collection resolutions for 1/16Hz airflow, 1mm PMMA thickness and an amplitude of 0.15m/s. Selected resolution is 2Hz.

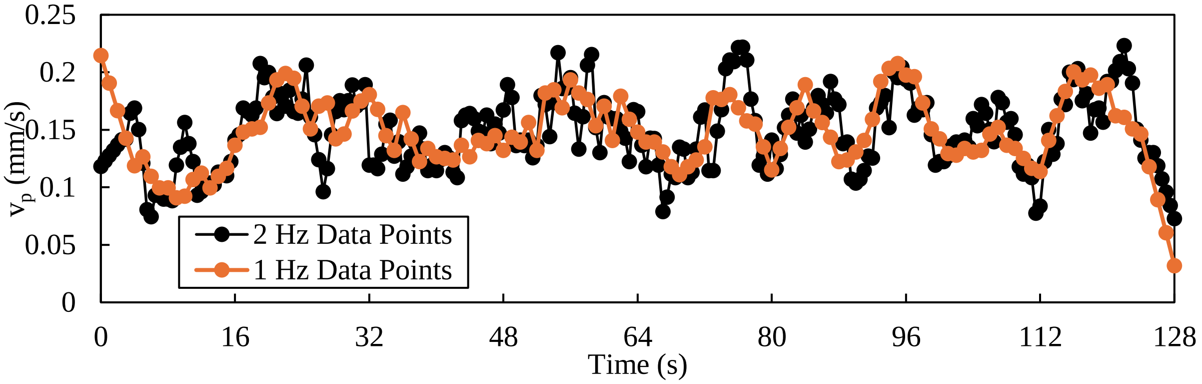

*Figure 32.* Flame spread results comparison between various data point collection resolutions for 1/32Hz airflow, 1mm PMMA thickness and an amplitude of 0.15m/s. Selected resolution is 1Hz.

## *Appendix C. Steady flow FFT of $v_p$*

An FFT analysis for the steady flow cases was performed on the transient $v_p$ to confirm that no frequencies are present in the baseline steady flow cases.

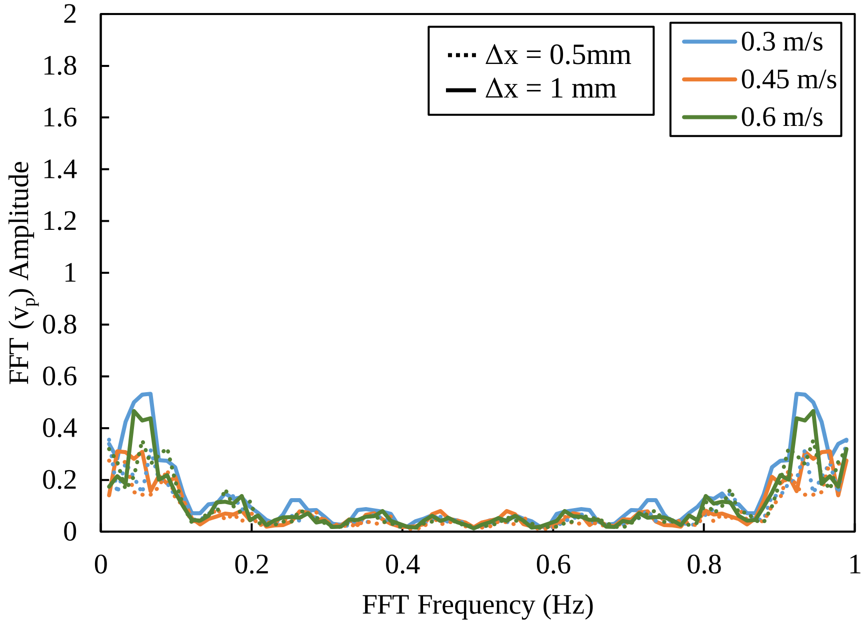

*Figure 33.* Average FFT results of the instantaneous spread rate for each steady flow case, to show that no significant peaks are observed in the steady cases. y-axis is scaled to the same values presented by the FFT results for non-steady cases (Figure 19).

## *Appendix D. FFT of change of $l_p$ over time*

Below are the results for an FFT analysis performed on the change in pyrolysis length ($l_p$) over time. The same process as the $v_p$ and $l_f$ analysis discussed in the results section was taken, and it reflects the same solid phase results observed in the $v_p$ analysis.

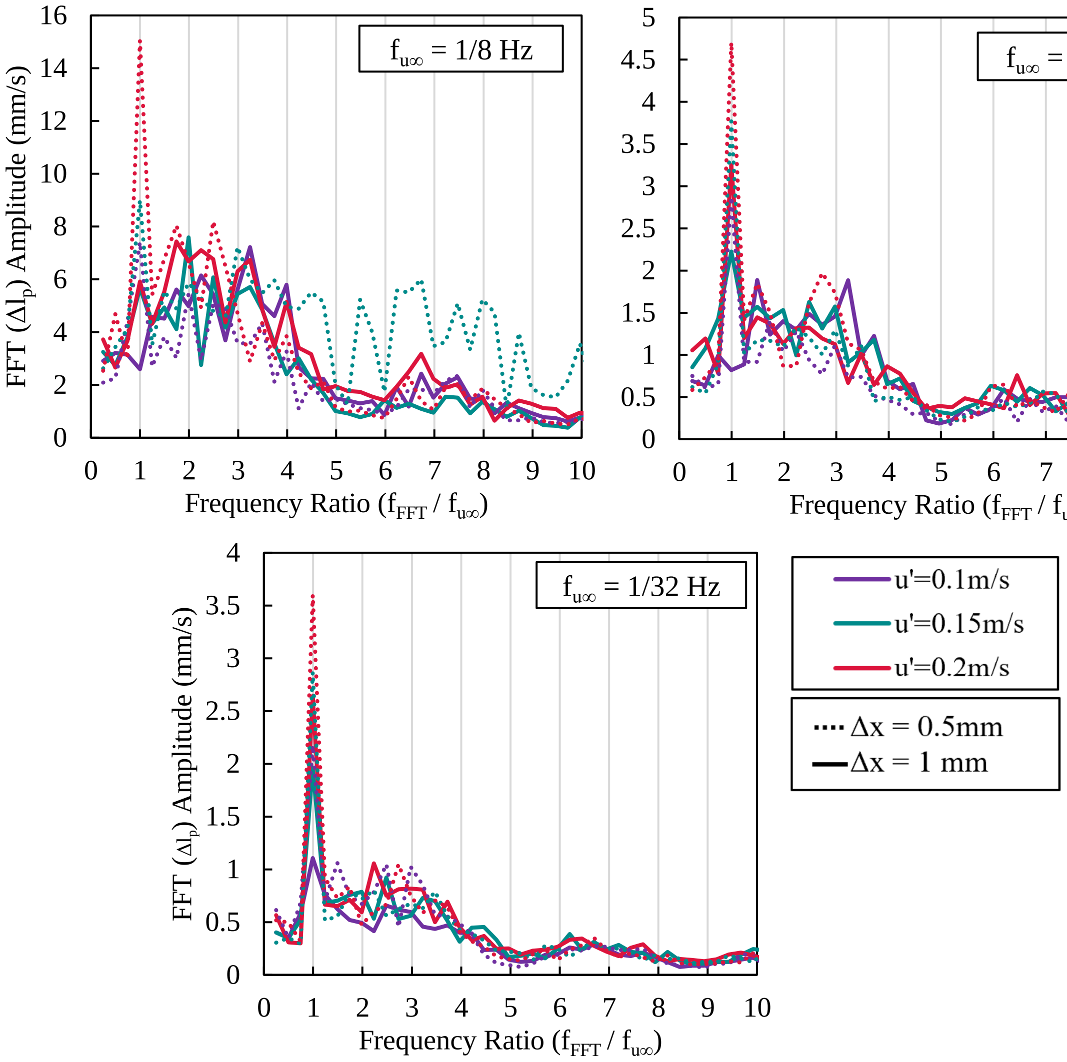

*Figure 34.* Averaged Fast Fourier Transform results on transient change in pyrolysis length over time for all non-steady test conditions. The FFT frequency is normalized by the opposed airflow frequency.

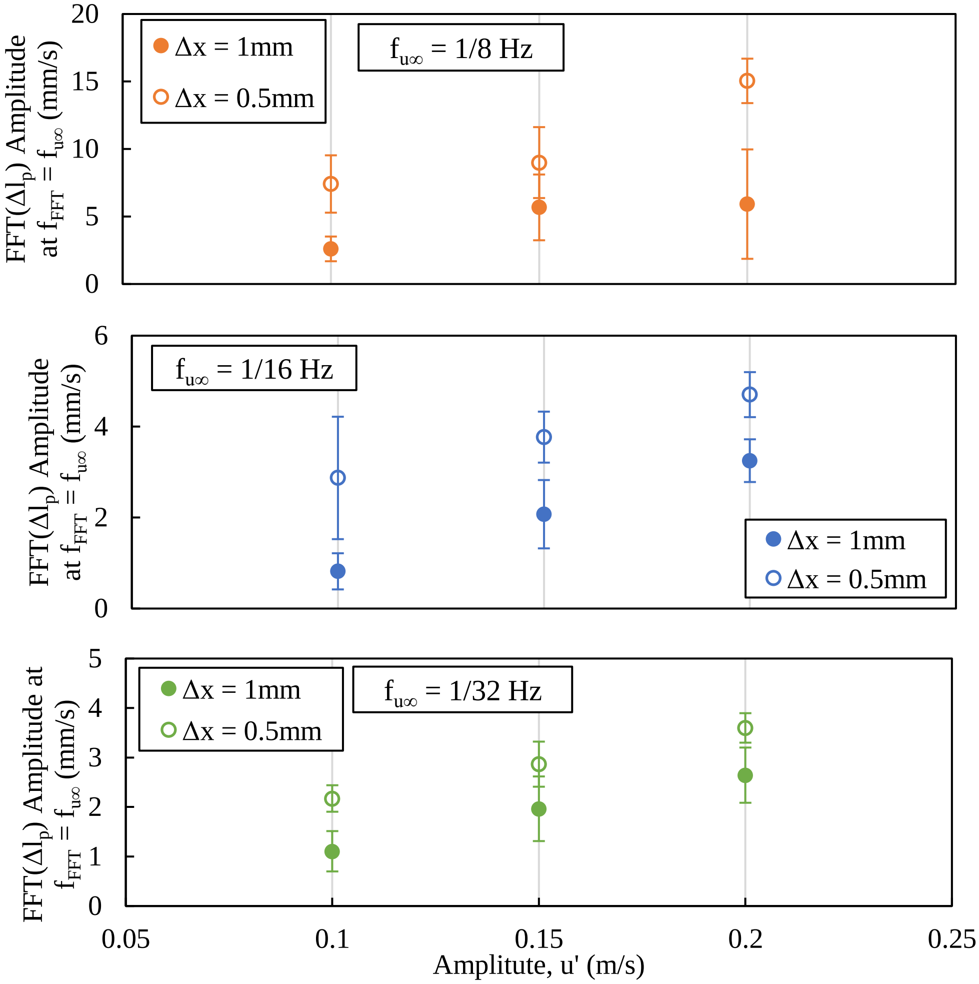

*Figure 35*. Magnitude of $\Delta l_p$ FFT amplitude at all opposed airflow conditions. Error bars are ± the standard deviation between replicate tests.